



Review

Laser-derived graphene: A three-dimensional printed graphene electrode and its emerging applications

Narendra Kurra ^{a,*}, Qiu Jiang ^{a,1}, Pranati Nayak ^{b,1}, Husam N. Alshareef ^{a,*}^a Materials Science and Engineering, Physical Science & Engineering Division, King Abdullah University of Science and Technology (KAUST), Thuwal, 23955-6900, Saudi Arabia^b Electrodes and Electrocatalysis (EEC) Biosensor Division, CSIR- Central Electrochemical Research Institute (CSIR-CECRI), Karaikudi, Tamilnadu, 630006, India

ARTICLE INFO

Article history:

Received 6 October 2018

Received in revised form 1 December 2018

Accepted 24 December 2018

Available online 2 January 2019

Keywords:

Graphene

Laser writing

Energy

Sensor

Electrocatalysis

Electronics

ABSTRACT

Printing of binder-free graphene electrodes directly on substrates has the potential to enable a large number of applications. Though conventional processing techniques such as ink-jet, screen-printing, and roll coating methods offer reliable and scalable fabrication, device performance has often been limited by re-stacking of the graphene sheets and by presence of passive binders and or additives. Laser-based, direct-write technologies have shown promise as a reliable, maskless, and template-free patterning method. Thus, laser-derived graphene (LDG) electrode is emerging as a promising three-dimensional graphene electrode that can be simultaneously derived from precursor carbons or polymers and patterned upon laser exposure. The LDG can be obtained through irradiation by a variety of laser sources including CO₂ infrared laser and femtosecond laser pulses, depending on the nature of the starting carbon precursors. Controlling the microstructure, amount and types of doping, and post-deposition methods enable a variety of applications including energy storage, catalysis, sensing and biomedicine. In this review article, we discuss recent progress in using laser-based fabrication of printed 3D graphene electrodes and its wide spectrum of applications. The review also discusses the material aspects of 3D graphene electrodes and provides an outlook for future potential.

© 2019 Elsevier Ltd. All rights reserved.

Contents

Introduction	82
On-chip graphene electrodes by laser technology	82
Laser-derived 3D graphene electrodes for electrochemical energy storage	85
graphene-based symmetric supercapacitors	86
Fabrication of on-chip micro-supercapacitors	87
Asymmetric micro-supercapacitors based on Printed (on-chip) 3D Graphene Electrodes	88
Effect of doping on electrochemical performance	89
On-chip biosensors	92
Heterogeneous electron transfer rates	92
Electrochemical biosensing	93
Nonenzymatic glucose detection	94
pH sensors	94
Electrocatalysis	94
Oxygen reduction/evolution reaction catalysts	95
HER catalysts	96

* Corresponding authors.

E-mail addresses: narendra.kurra@kaust.edu.sa (N. Kurra),husam.alshareef@kaust.edu.sa (H.N. Alshareef).¹ Equal contribution.

Other exotic applications	96
Antifouling properties.....	97
Electroacoustic applications	98
Outlook and perspectives.....	99
Acknowledgment.....	100
References	100

Introduction

Graphene has attracted significant attention from the research community due to its fascinating physicochemical properties [1–10], making it suitable for a wide range of applications ranging from nanoelectronics to energy storage [11–20]. High crystalline quality graphene (e.g., graphene obtained through mechanical exfoliation of the bulk graphite) is key to its superlative properties including massless ultrahigh mobility of charge carriers ($\tilde{1}0^5 \text{ cm}^2/\text{Vs}$) [21–25], high optical transparency (~97.7%) [26], excellent thermal conductivity (~5 kW/mK) [22], high mechanical strength (1 Tpa) [12] and large theoretical surface area (~2630 m²/g) [27]. Thermally-intensive processes, such as chemical vapor deposition (CVD) and thermal decomposition of silicon carbide, resulted in the growth of high crystalline quality graphene with negligible defects [23,28–31]. However, the high thermal budget involved in such processes limits the type of substrates that can be used for direct growth of graphene, and often a transfer process is needed to make devices on substrates that cannot withstand high temperatures (e.g., plastic substrates). Therefore, rational design and scalable processing of functional graphene materials at low temperatures on a variety of substrate platforms have attracted significant interest recently [10,20]. The trend toward developing cost-effective graphene materials enabled the ease of fabrication of functional sensors, electrocatalysts and energy storage devices [4,14]. However, the bottleneck lies in the ‘restacking’ of graphene sheets through spontaneous van der Waals and π - π interactions in a solution processable route [32], posing a challenge in developing graphene-based open frameworks.

Engineering native 2D graphene sheets into monolithic three-dimensional (3D) porous architectures has become important during the past decade due to the multitude of applications, including the fabrication of on-chip functional graphene devices. Conventional CVD has been widely employed for making 3D graphene foams but lacks scalability due to the associated growth process followed by etching of the metal scaffold [33]. In this scenario, solution processing of functionalized graphene has become attractive as it offers compatible coatings on a variety of substrates in an inexpensive yet scalable manner [34]. Hummers’ method typically relies on oxidation of bulk graphite powders, which enables a natural dispersion of graphene oxide (GO) sheets with surface polarity and hydrophilicity [35]. Self-assembly of such functionalized graphene materials enabled fabrication of 3D foam structures; however, they suffer from the insulating nature of GO [36,37]. To recover the electronic conductivity, a wide variety of reduction protocols including chemical, thermal, and solvothermal were developed [3,16,38]. These reduction protocols were only intended to reduce the GO; additional deposition and patterning protocols should be adopted to fabricate on-substrate graphene electrodes. Therefore, it is important to develop a strategy that involves simultaneous reduction, exfoliation, and printing of 3D graphene electrodes into desired patterns on relevant substrates for many potential applications [8,39–43].

Laser scribing technology based on consumer-grade digital video disc (DVD) burners has shown significant promise as a solid-state approach for scalable fabrication of graphene-based devices

from GO films in a single step [44]. It enabled simultaneous reduction of GO while generating desired electrode patterns in a scalable manner. The laser scribing technique facilitated controllable fabrication of 3D architectures from 2D stacked GO layers. Distinctively, Tour group pioneered the fabrication of graphitic carbon from commercial polyimide through CO₂ laser irradiation and extended this concept to a variety of natural and synthetic carbon precursors [45]. This strategy offered direct formation of conductive and 3D porous graphitic electrode patterns on insulating polymer substrates, avoiding the additional step of processing the GO. Unlike using the mild source of the DVD burners for the laser reduction, the CO₂ laser is highly energetic and can transform natural carbon sources into graphitic materials without the need for metal catalyst layers. Since the laser converts carbon precursors into the graphitic material, this technique is referred to as laser-induced graphene (LIG); a recent review article reports progress in this field [45]. The noteworthy point here is that ‘graphene’ nomenclature was often used for both LSG (laser-scribed graphene) and LIG (laser-induced graphene), even though they are not a strictly single sheet of sp^2 carbon lattice. The LSG and LIG terminologies have been used in the literature reports, however, we propose the use of “laser-derived graphene (LDG)” as a generic term for the laser-based formation of printed graphene electrodes, independent of the laser type or precursor material used. Such kinds of graphitic architectures may not have the same electronic quality as that of graphene obtained from mechanical exfoliation or high-temperature growth methods, but they are suitable for a variety of applications requiring printed patterns of 3D graphene. Based on the laser conditions and the nature of carbon precursors, it is possible to control the microstructure, functionality, defect density and thus the associated properties of LDG electrodes.

In this article, we review recent progress on laser-derived 3D graphene electrodes and their emerging applications in the fields of energy storage, electrocatalysis and sensing (Fig. 1). We start by summarizing the historical evolution of using laser-based techniques for the formation and direct patterning of graphene. We discuss both laser-induced reduction of GO to patterned graphene devices and laser-induced transformation of polymeric and other natural carbon sources into 3D graphene architectures. We then review the key lasing parameters and precursor that determine the structure and properties of the resultant graphene patterns and the versatile applications of LDG electrodes.

On-chip graphene electrodes by laser technology

The simultaneous formation and patterning of graphene on a substrate (SiO₂/Si, plastic, glass, and paper) is referred to as “on-chip graphene electrode” and is typically a binder-free monolithic architecture. Historically, the thermal atomic force microscope (AFM) probe was employed to fabricate ~10 nm wide graphene nanoribbons by local thermal reduction of GO [46]. The low-throughput nature of AFM limited the scalability of this technique; however, it could lead to the use of laser technology to make scalable graphene patterns. Laser technologies have been extensively employed in patterning and growth of nanostructured materials via maskless and transfer printing routes [47,48]. For instance, Kurra

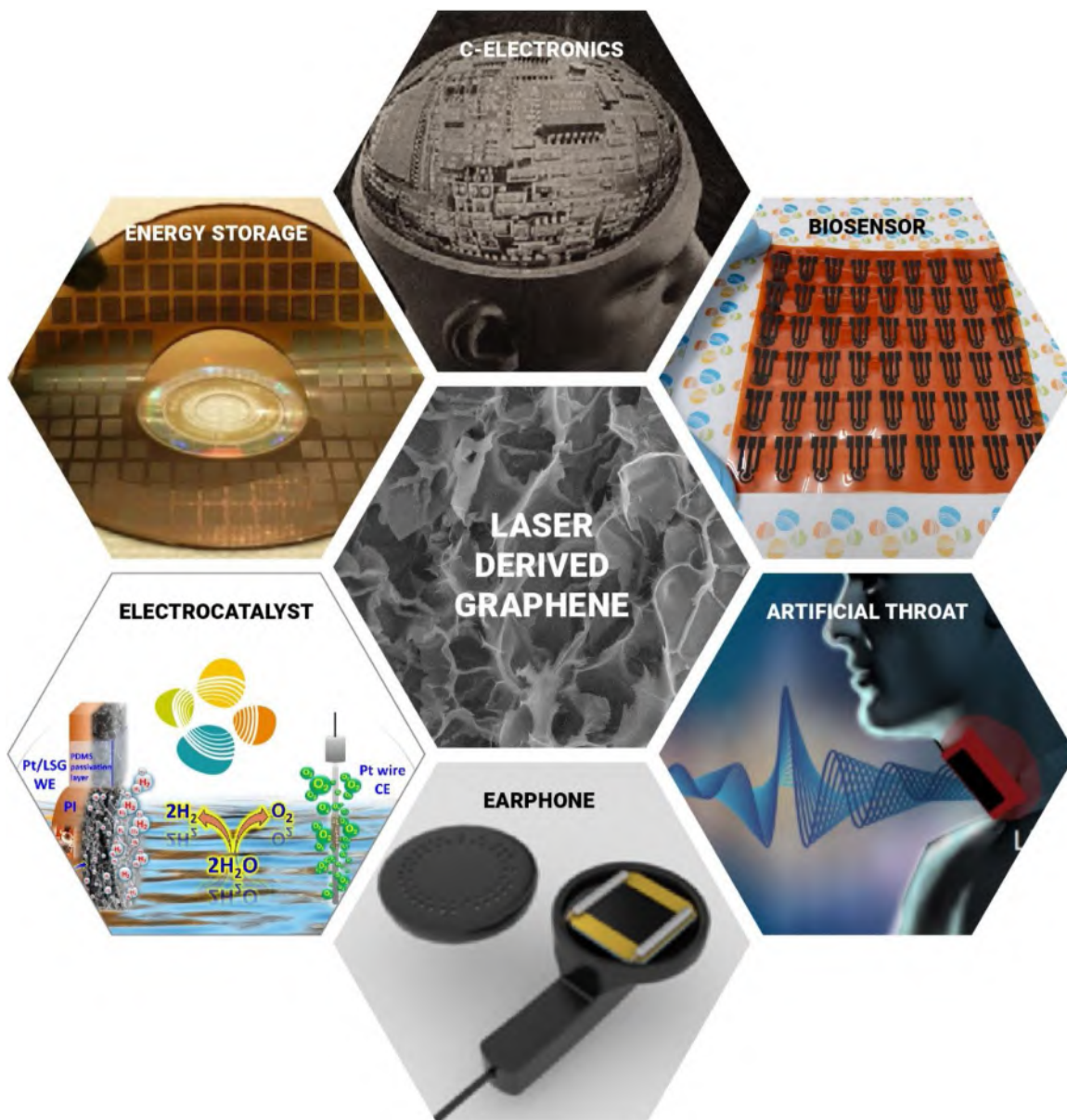


Fig. 1. Emerging electronics and electrochemical applications of laser-derived graphene architectures. Adapted with permissions from reference [65,69,70,72,73,81].

et al. employed pulsed laser interference ablation for direct patterning of graphite surfaces, which they then used as a source for obtaining graphene ribbons [49]. Laser processing was also employed for rapid synthesis of graphene structures in a catalyst-free manner [50]. Pulsed laser sources were not only employed as tools for patterning graphite surfaces but also used for reducing GO. A variety of laser sources including femtosecond, nanosecond, Nd: YAG, CO₂, diode, krF, and fiber types have been employed for reducing GO photothermally [51–64]. A focused laser beam provides highly controlled heating/cooling rates compared to conventional annealing procedures, enabling rapid fabrication of graphene-based devices. Concurrently, the high path length of the laser beam induces localized heating in selected areas with micron size precision [45].

In 2012, Kaner et al. pioneered an inexpensive solid-state approach for reducing GO films using an ordinary DVD laser burner [65]. Commercial LightScribe drives are inexpensive (~\$20) and can be controlled by a standard desktop computer. The LightScribe program allows control of the intensity or power of an IR laser beam

(wavelength = 788 nm, maximum power output = 5 mW) inside the optical drive by pulsing through an objective lens. This technique is based on producing photothermal effects (the temperature may range from 300 to 500 °C) through an IR laser beam to volatilize the functional groups on the GO surface and produce conductive reduced GO. This DVD LightScribe technique enabled selective reduction of GO without the need for a mask, which led to the fabrication of many graphene-based electronics and energy storage devices [44,65–68]. To demonstrate the complex patterning capability of LightScribe technology, intricate circuit designs were sculpted on a man's head by reducing GO film accordingly with laser scribing (Fig. 1) [52,69–73]. This technique has the potential to create complex patterns without using masks, templates or post-transferring protocols. Additionally, LSG-metal or LSG-metal oxide composite structures were fabricated using this technology, demonstrating the versatility in printing graphene and its composite electrodes directly on a substrate without using external masks.

Table 1

Summary of laser technologies used to produce graphene architectures from various carbon sources and their potential applications [44,52,54,63–65,72,74–88].

Carbon source	Laser type	Power	Application	References
GO	LightScribe DVD burner	788 nm, 5mW	Supercapacitor	[44,65]
		N/A (HP inc. 557S)	Transistor Loudspeaker Photodetector	[79]
GO	650 nm laser	788 nm, 5mW	RRAM	[82]
		N/A (HP inc. 557S)	Pressure sensor	[80]
		788 nm, 5mW	LED	[77]
GO	450 nm laser	788 nm, 5mW	Earphone	[81]
		143 μW, 8.49 mm ⁻¹	Heater	[86]
		90 mW, 8.5 mm ⁻¹	Strain sensor	[78]
GO	248 nm UV laser	0.13 mW, 7mm ⁻¹	Sound sensor	[83,84]
		48–240 mJ/cm ²		
		N/A (Hewlett-Packard Inc.)	N/A	[63]
GO	788 nm CW laser	47–968 mJ cm ⁻²		
GO	800 nm femtosecond laser	200 mW	Photodetector	[85]
GO	650 nm laser	5–80 mW, 50 μm s ⁻¹	N/A	[88]
PI	532 nm DPSS laser	500 mW, 8.5 mm ⁻¹	Intelligent throat	[72]
PI, PEI	450 nm Laser	2.4–5.4 mW, 3.5 inch s ⁻¹	Supercapacitor	[52]
PI	10.6 μm CO ₂ pulsed laser	6 mW	Strain sensor	[64]
SPEEK	CO ₂ pulsed laser	6 W, 500 mm ⁻¹	Supercapacitor	[54]
Paper, coconut, bread, potato, etc.	Ar–Kr laser, 514.5 nm	3.75 W, 15 cm s ⁻¹	N/A	[74]
Teflon	10.6 μm CO ₂ pulsed laser	5 W, 15 cm s ⁻¹	N/A	[76]
CH ₄ , H ₂	532 nm OPSS laser	5 W	N/A	[87]
Wood	10.6 μm CO ₂ pulsed laser	7.8 W	Electrocatalyst	[75]

GO: graphene oxide; **DVD:** digital video disc; **UV** laser: ultraviolet laser; **CW** laser: continuous wave laser; **DPSS** laser: diode-pumped solid-state laser; **OPSS** laser: optically-pumped solid-state laser; **PI:** polyimide; **SPEEK:** sulfonated poly(ether ether ketone); **CH₄:** methane; **PEI:** polyetherimide.

Lin et al. recently developed an innovative approach for writing graphene patterns on commercial polyimide (PI, Kapton) films using a CO₂ laser cutting tool usually found in machine shops [52]. This process is based on the photothermal transformation of sp³ carbon atoms into an sp² carbon lattice by laser irradiation. In contrast to an IR laser beam, the CO₂ laser can produce temperatures >1000 °C, which is responsible for graphitizing the polymer under ambient conditions, without the need for a metal catalyst. Furthermore, this process was used to transform polysulfone membrane polymers into sulfur-doped LIG [71], demonstrating the versatility of this approach. By optimizing laser parameters and choosing the appropriate gas environment, it was demonstrated that a variety of natural materials including wood, food, paper, and cardboard were transformed into LIG structures [74,75]. Fluorinated diamond and fluorinated graphene were recently synthesized from Teflon (polytetrafluoroethylene) via laser-induced transformation [76]. Table 1 summarizes the laser-based technologies that have been used for producing graphene-based patterns either from GO, polymers or natural resources and their wide range of applications [44,52,54,63–65,72,74–88].

In this review article, we emphasize two types of direct-write laser technologies that can be used to generate 3D graphene electrode patterns directly on substrates: (i) conversion of GO into conductive reduced GO using an IR laser similar to those found in DVD technologies, and (ii) conversion of polymers and natural carbon sources into graphitic carbon using a CO₂ laser. These two laser techniques share common aspects that offer direct-write (maskless) fabrication of printed 3D graphene electrodes. In the following sections, we discuss progress on the formation of these 3D printed graphene electrodes and their applications in carbon electronics, electrochemical capacitors, sensors, electrocatalysts and bio-medical applications (Fig. 1).

The unique aspect of the laser technique is the photothermal conversion or transformation of nonconductive carbon materials into conductive graphitic structures. The laser power is determined by the type of laser, spot size and other instrumental parameters that can control the localized temperature profiles. The instantaneous temperature rise in the lasing area influences the choice between the molecular and atomic structure of the carbon. For

instance, the conductivity of GO film was enhanced by five orders of magnitude (typical sheet resistance of GO films >20 MΩ/sq to highly reduced GO films 80 Ω/sq) through optimized lasing conditions [44]. The phenomenon involves the release of oxygen-containing functional groups (CO, CO₂) on instantaneous heating of GO film, with the subsequent expansion of stacked GO to expanded grapheme structure. The local pressure created by the liberated gases causes protruded graphene morphology, which is evident in the SEM micrograph in Fig. 2a-d [44]. A very similar phenomenon occurs in the case of a polyimide substrate or thin polymeric films. Here, the viability of the CO₂ laser to create localized temperatures above 1000 °C could induce graphitization at depths of a few tens of microns. The method involves the direct synthesis of graphene from polymeric substrates without requiring pre-synthesized GO (a typical precursor material for LSG technology) and produces a highly conductive graphene scaffold (sheet resistance 10–100 Ω/sq) [52].

Since the quality of graphene formed by direct laser irradiation influences the device performance, it is crucial to investigate the morphology, electrical conductivity, surface functionality, specific surface area, and chemical nature. The instantaneous heating and simultaneous release of gaseous byproducts turn both GO- and PI-derived graphene into a highly porous 3D electrode rich in edge plane sites, as depicted in Fig. 2a-d. The quality and defects of graphitic carbon can be quantified using Raman analysis (Fig. 2e, f). Raman spectroscopy is one of the most sensitive and informative techniques to characterize disorder in the sp² carbon lattice. In graphene-based materials, the Raman spectrum predominantly consists of three peaks which are referred to as D, G, and 2D bands [89–91]. The extent of the reduction of GO after laser irradiation can be inferred from the position, shape, full width at half maxima (FWHM) and the ratio of the peaks with respect to the GO. The D band originates from the breaking of the translational symmetry of the sp² carbon lattice, the G band from the stretching vibration of the sp² carbon lattice, and the 2D band from the stacking of graphene sheets along c-axis. I_D/I_G ratio can be used to estimate the defect density and the shape of the 2D band reveals the nature of the stacking of graphene sheets. The narrow D and G bands after laser exposure of GO and the appearance of the 2D band indicates a significant reduction of GO into the graphitic structure with c-axis

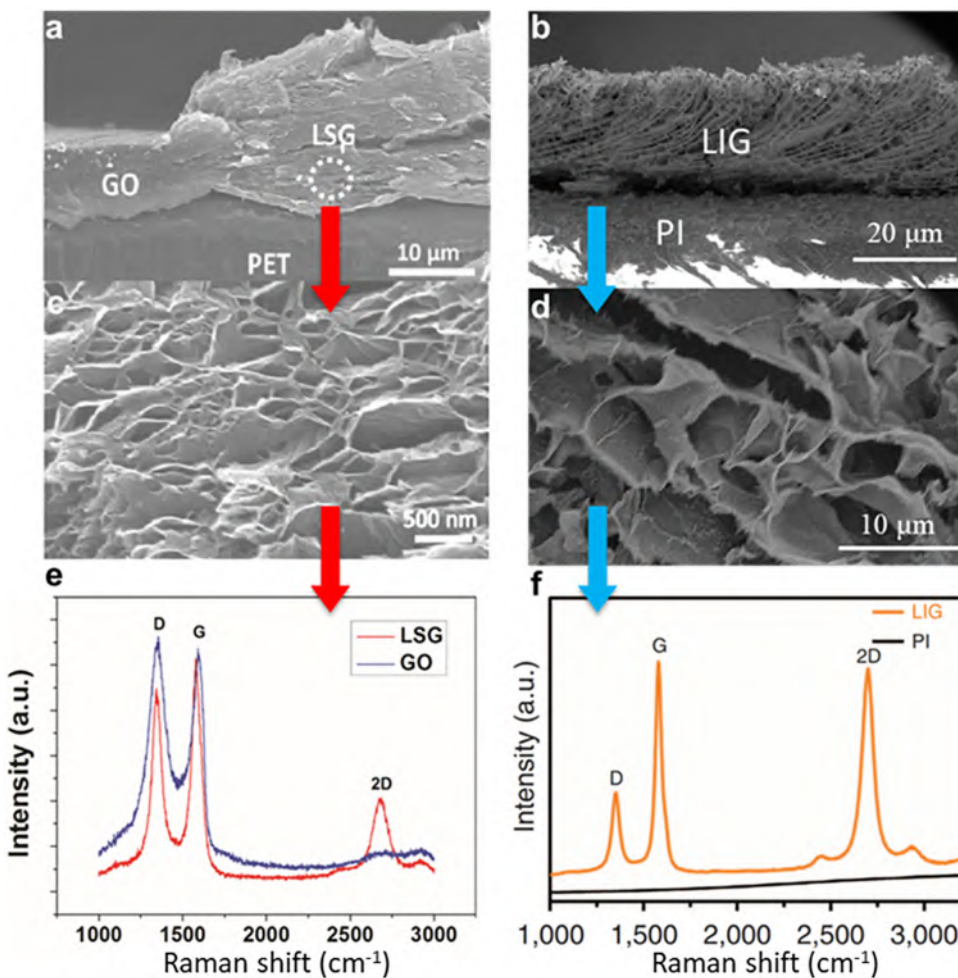


Fig. 2. SEM micrographs of (a) LSG and (b) LIG. Corresponding magnified cross-sectional SEM images are shown in (c) and (d). Raman spectra are presented in (e) and (f), respectively. GO: graphene oxide, LSG: laser-scribed graphene, PI: polyimide, LIG: laser-induced graphene. Adapted with permissions from reference [44,52].

periodicity (Fig. 2e). As detailed in a recent review article, insight into GO reduction by laser irradiation was analyzed and quantified using infrared, X-ray photoelectron and UV-vis spectroscopies [92]. The Raman spectrum of graphene derived from polyimide displayed intense and narrow peaks corresponding to the D, G, and 2D bands, confirming that polyimide transforms into graphene under CO₂ laser irradiation. The degree of graphitization can be controlled by the appropriate choice of laser power [52]. Since a CO₂ laser produces higher temperatures compared to a DVD burner, the degree of graphitization is superior in the former. Other natural carbon sources such as bread, coconut shell and wood were graphitized using the right choice of CO₂ laser parameters and environments.

The key features of the LDG include a porous conductive scaffold with abundant defect sites, which is beneficial for efficient transport of electrolyte ions and electrons. This makes it an excellent printed 3D electrode for electrochemical applications. It is noteworthy that these LDG electrodes do not require any binders for electrochemical applications. Such binders can block some of the electrochemical sites and influence the intrinsic electrochemical properties of carbon-based materials. Thus, the laser-formed printed graphene electrodes could offer a significant advantage in electrochemical applications. In the following sections, we review several applications that capitalize on the advantages of printed 3D graphene electrodes to improve electrochemical performance over re-stacked graphene layers.

Laser-derived 3D graphene electrodes for electrochemical energy storage

The rapid growth in miniaturized electronics and self-powered sensors demands the development of small-scale energy storage units [93]. For instance, implantable biochips, radio frequency identification (RFID) tags, environmental sensors, nanorobotics and microelectromechanical systems (MEMs) need compatible micro-power sources [93,94]. In addition, the energy autonomy requires the development of harvesting units to transform intermittent renewable sources, such as solar, wind and thermal, into a continuous power supply over prolonged periods for “self-sufficiency”.

On-chip energy storage is the advanced version of electrochemical energy storage to cope with miniaturized electronics. Thin film batteries and micro-batteries have been commercialized, but they suffer from limited lifetime and low power density [95–97]. Since micro-supercapacitors offer an essentially infinite lifetime with higher power density than micro-batteries, they are suited for applications including remote sensing networks, implantable sensors and the internet of things (IoT) [94]. In such devices, the harvested energy may be intermittent while providing non-constant voltage output with time [98]. Since batteries often require constant voltage output for charging, micro-supercapacitors can be charged more efficiently by drawing the maximum current supply from the source, irrespective of voltage output [98,99].

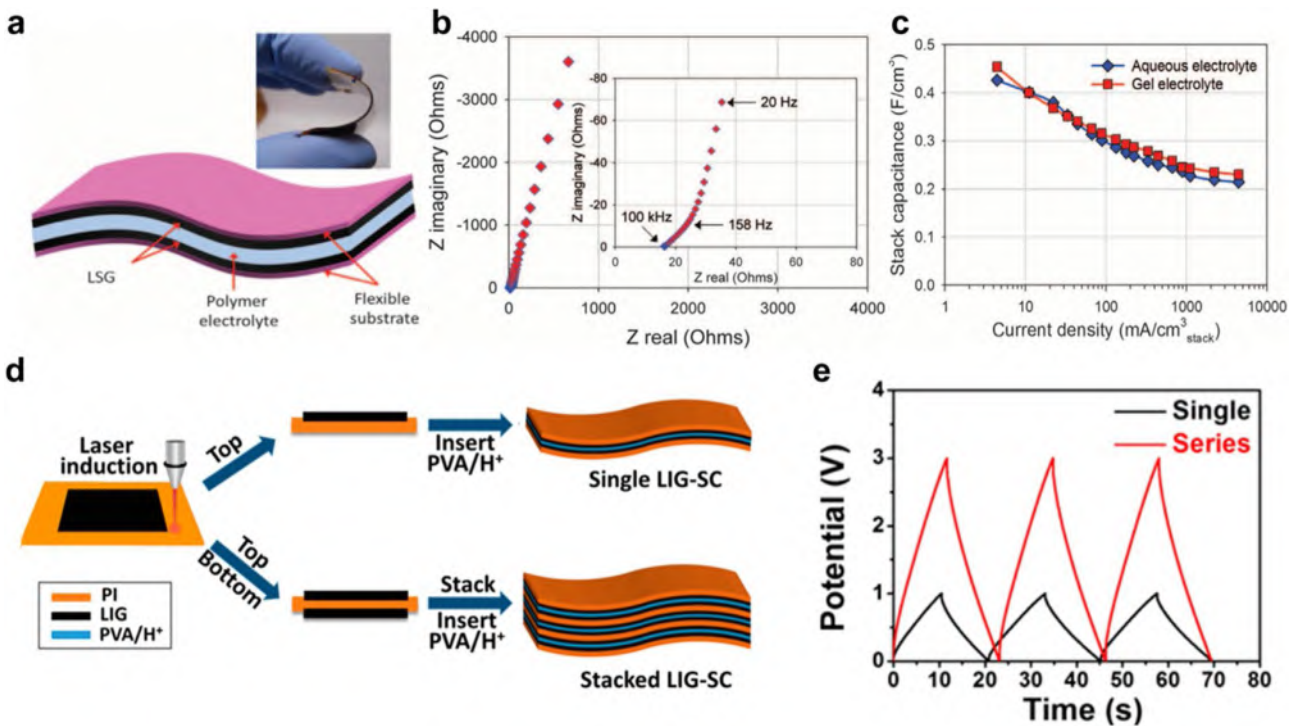


Fig. 3. Laser-derived graphene electrodes for electrochemical capacitors. (a) A cross-sectional view presenting the LSG electrodes supported on a flexible substrate. (b) Impedance plot of an LSG sandwich supercapacitor in 1 M H₃PO₄. (c) Comparison of stack capacitance of LSG supercapacitors in aqueous and gel electrolytes. Adapted with permission from reference [44]. Copyright 2012, American Association for the Advancement of Science. (d) Stackable series and parallel connected LIG solid-state supercapacitors. (e) Charge-discharge profiles of single and series connected LIG supercapacitors. Adapted with permission from reference [113]. Copyright 2015, American Chemical Society.

The typical layout of a micro-supercapacitor may include either thin film or planar interdigitated electrode architecture, but the latter has advantages such as faster electrolyte ion movement, high power and rate capabilities, and easier on-chip integration [100,101].

The field of micro-supercapacitors is evolving rapidly [102]. As far as the materials are concerned, carbon is earth-abundant and cheap; various nanostructured carbon materials have thus been explored as micro-supercapacitor electrodes. Activated carbon, onion-like carbon, carbide-derived carbons, carbon nanotubes, and graphene were employed in fabricating micro-supercapacitors [103–107]. Various pseudocapacitive electrode materials including transition metal oxides, nitrides, carbides and conducting polymers have also been explored. There are excellent review articles describing the progress on micro-supercapacitors [94,95,101,102,108,109]. Most of the micro-supercapacitors were fabricated using standard microfabrication methods, which involve a multi-step protocol and expensive infrastructures such as a mask aligner and a sophisticated cleanroom. Therefore, direct and scalable fabrication of micro-supercapacitors with minimal infrastructure is a requirement for low-cost solutions.

graphene-based symmetric supercapacitors

Gao et al. employed a laser technique to selectively write reduced GO patterns directly on GO free-standing film [51]. The laser-reduced GO was used to form an electrode material pattern, while the hydrated GO served as an ionic conductor in fabricating planar graphene electrochemical capacitors. However, the electrical and ionic conductivities were not sufficiently high, causing poor frequency response and large internal resistance (6.5 kΩ) of the as-made graphene devices with GO as an ionic conductive medium.

Initial efforts have been focused on synthesis of graphene oxide, and ways to reduce it for electrochemical energy storage applications [110–112]. Kaner's group pioneered the process of GO reduction by laser scribing graphene electrodes using a standard LightScribe DVD optical drive method [44]. Their work illustrated that irradiation of GO film with an IR laser resulted in mechanically robust and electrically conducting (17.4 S/cm) films with a specific surface area of 1520 m²/g. They used this approach to fabricate a printed flexible electrochemical capacitor without binders or current collectors (Fig. 3a). They optimized laser parameters to achieve lower equivalent resistance values in their LSG supercapacitors (Fig. 3b). Furthermore, their supercapacitors delivered a power density of 20 W/cm³, which is almost 20 times higher than activated carbon-based supercapacitors. As illustrated in Fig. 3c, the flexible solid-state supercapacitors were made using poly(vinyl alcohol)-phosphoric acid (PVA/H₃PO₄) gel electrolyte, which gave a similar electrochemical performance to that of liquid electrolyte. This is mostly because of the porous LSG electrode structure, which allowed the gel electrolyte to penetrate deep into the electrode.

Peng et al. demonstrated vertically stacked graphene supercapacitors by transforming both sides of polyimide sheets into porous graphene through laser irradiation [113]. The advantage of this fabrication method is that the 3D graphene electrodes can be produced under ambient conditions in which the remaining PI layer at the middle separates the graphene electrodes, enabling the fabrication of vertically integrated supercapacitors to enhance the volumetric electrochemical performance while preserving the device flexibility (Fig. 3d). These supercapacitors can be integrated into series and parallel connections to meet the required power ratings. Compared to single devices, series connected micro-supercapacitors exhibit three times higher voltage window (Fig. 3e), demonstrating the ability of the laser technique to manufacture integrated

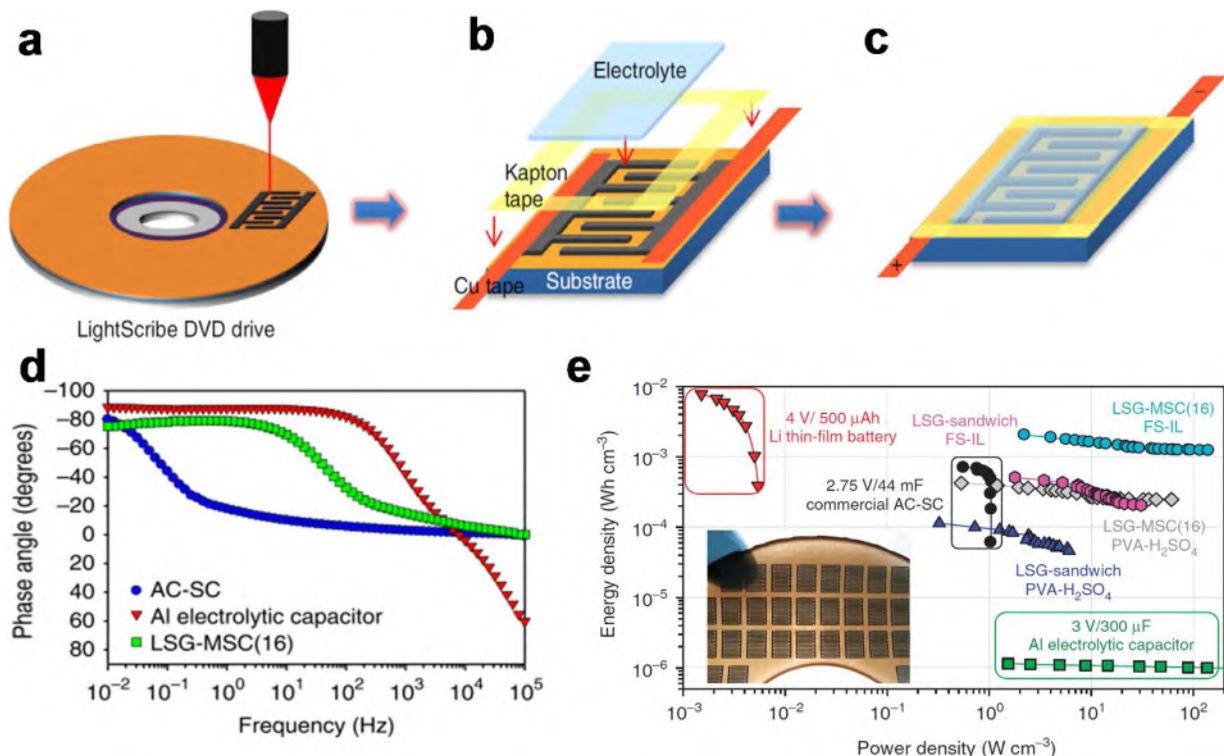


Fig. 4. (a-c) Schematic illustrating the fabrication of an LSG micro-supercapacitor. (d) Phase angle versus frequency of LSG MSC in comparison to electrolytic and activated carbon-SCs. (e) Ragone plot comparing the electrochemical performance of LSG micro-supercapacitors with the state-of-the-art Li thin film batteries and electrolytic capacitors; the inset displays potential scalability of the laser scribing technique in producing more than 100 devices in a single run. Adapted with permission from reference [65]. Copyright 2013, Springer Nature.

graphene-based supercapacitors according to the need for output current/voltage ratings.

Fabrication of on-chip micro-supercapacitors

Laser techniques allow planar fabrication of graphitic electrodes, enabling the direct fabrication of LDG micro-supercapacitors. El-Kady et al. have demonstrated the scalable fabrication of graphene micro-supercapacitors over large areas by direct laser writing on GO films using a standard LightScribe DVD burner [44,65]. They fabricated flexible micro-supercapacitors for powering up flexible electronics but also showed promise for on-chip integration with Microelectromechanical systems (MEMS) or complementary metal-oxide-semiconductor(CMOS) technologies. The laser scribing method offered the fabrication of a single device in 18 s. As illustrated in Fig. 4a-c, the direct ‘writing’ technique does not require masks and can be done in a regular laboratory environment without the need for a clean room. The presence of a GO layer in the interspaces between reduced GO serves as a separator and electrolyte (provided with enough ionic conductivity) for the all-carbon micro-supercapacitor. They also fabricated an array of micro-supercapacitors (>100) on a single piece of GO film deposited on a DVD. A lateral spatial resolution of $\sim 20\text{ }\mu\text{m}$ was demonstrated using this LightScribe method. Remarkably, these micro-supercapacitors exhibited three times higher energy and 200 times higher power compared to commercial activated carbon supercapacitors. These devices even exhibited higher power density than micro-batteries and higher energy density than electrolytic capacitors. Higher power densities could likely be achieved by reducing the ion-diffusion pathways through the selection of smaller width and spacing between the micro-electrodes. It is evident that the phase angle response of LSG MSCs is far better than that of commercial

activated carbon supercapacitors and approaching electrolytic capacitor performance (Fig. 4 d). Laser scribing technology has enabled an expanded open structure of graphene in which the distributed nature of the charge can be minimized, unlike in the case of microporous carbon electrodes. Furthermore, LSG MSCs delivered higher energy density at high charge-discharge rates than state-of-the-art micro-supercapacitors (Fig. 4e).

Li et al. employed a femtolaser-reduction process to pattern both rGO electrodes and Au current collectors in a single step to improve the conductivity of rGO electrodes [100]. Unlike continuous wave lasers, femtosecond lasers can induce multiphoton polymerization, reduction, melting and etching of different categories of materials. For instance, the strong peak power of ultrashort pulses enables a nonlinear multiphoton interaction with the materials within the focal point, which may be beneficial for obtaining composites of rGO. In this study, hydrated GO and chloroauric acid nanocomposite film was reduced in-situ by exposing them to the femtosecond laser beam to create rGO/Au micropatterns. The conductivity of rGO/Au (1100 S/cm) was improved by two orders of magnitude compared to rGO alone, resulting in improved rate capabilities (volumetric capacitance of 10.2 F/cm^3 at high scan rate of 100 V/s) and power densities (time constant of 2.76 ms) over rGO-based micro-supercapacitors fabricated by the femtosecond laser technique.

Hwang et al. demonstrated the synthesis and processing of LSG/RuO₂ nanocomposite electrodes through laser-induced redox reactions between precursors, GO and RuCl₃ [67]. This approach enabled the single-step fabrication of binder-free, metal current-collector-free graphene/RuO₂ interdigitated electrodes. The laser technique has also enabled the fabrication of integrated devices in series and parallel configurations to meet required power ratings. The laser scribing tool thus offers flexibility in fabricating hybrid graphene electrodes through the pre-selection of desired GO-composite material.

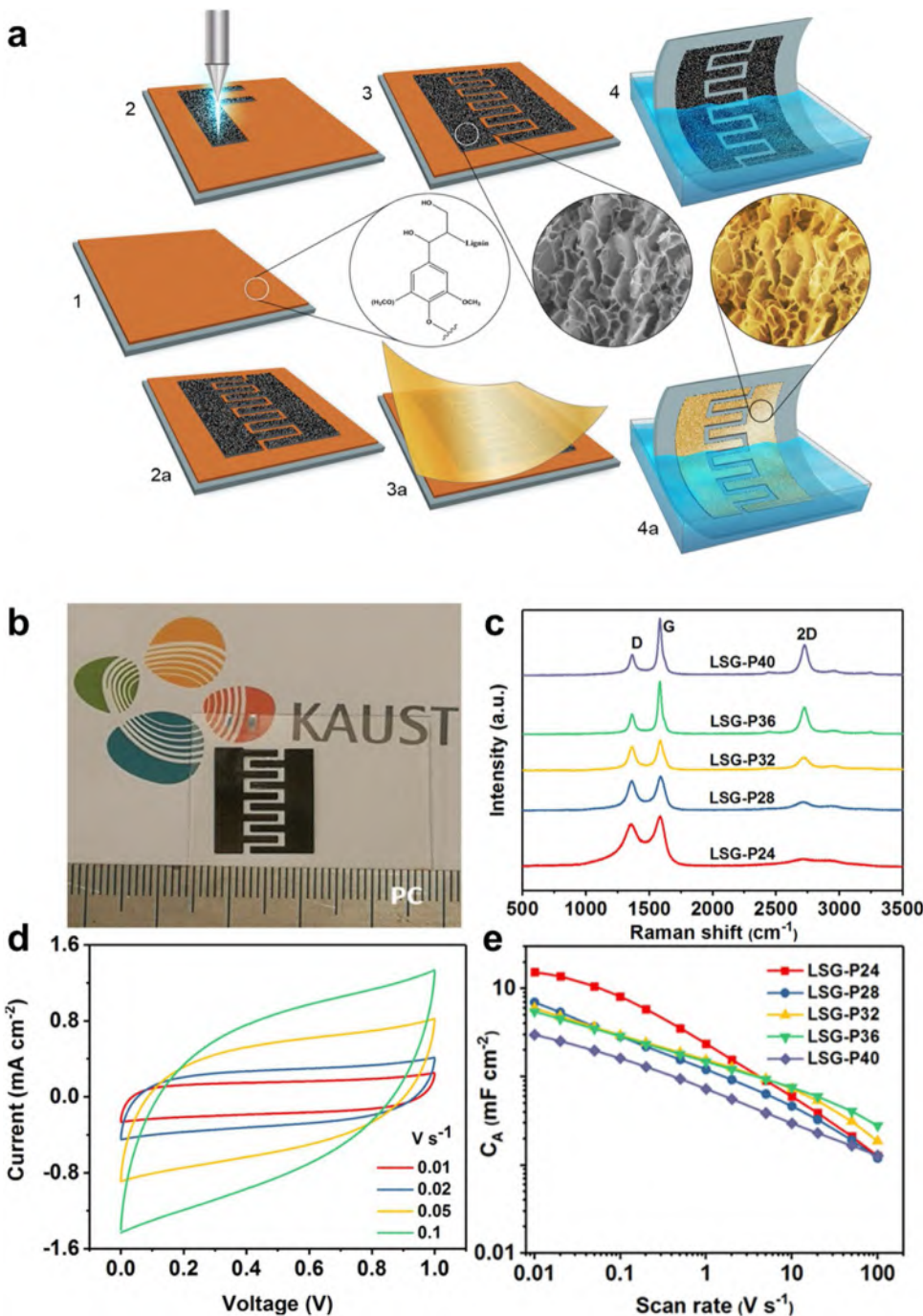


Fig. 5. (a) Schematic illustration for laser writing of 3D graphene patterns on lignin surface via lift-off in a water bath for micro-supercapacitor fabrication. (b) Digital photograph of the micro-supercapacitor on polycarbonate (PC) substrate. (c) Raman spectra presenting the dependence of laser parameters on the nature of the graphitic carbon produced. (d) Cyclic voltammograms of an optimized LDG micro-supercapacitor. (e) Comparison of corresponding electrochemical performance of LDG MSCs fabricated using different laser powers. Adapted with permission from reference [114]. Copyright 2018, Wiley-VCH.

Zhang et al. recently demonstrated laser lithography on lignin, which is an abundant natural polymer that exists in plants (Fig. 5a,b) [114]. Lignin is generally considered to be useless plant extract but transforming it into a useful product has both environmental and commercial significance. Laser conditions were optimized to convert lignin film into conductive graphitic patterns followed by lift-off in water to remove unexposed lignin regions (Fig. 5c). The electrochemical performance of LDG electrodes was then compared in a symmetrical configuration, as illustrated in Fig. 5d and 5e. These symmetric devices displayed areal capacitance values in the range of 3–10 mF/cm² at a scan rate of 10 mV/s, indicating that the capacitance values can be raised as much as three

times through optimized graphitic carbon electrodes. Importantly, all these LDG devices displayed rate capabilities up to 100 V/s, which is likely useful for high rate applications. The versatility and environmental friendliness of lignin laser lithography can inspire both the fabrication of graphene-based MSCs and the sustainable utilization of lignin.

Asymmetric micro-supercapacitors based on Printed (on-chip) 3D Graphene Electrodes

Aqueous symmetric supercapacitors have a limited cell voltage (<1 V), necessitating the development of a high operating voltage

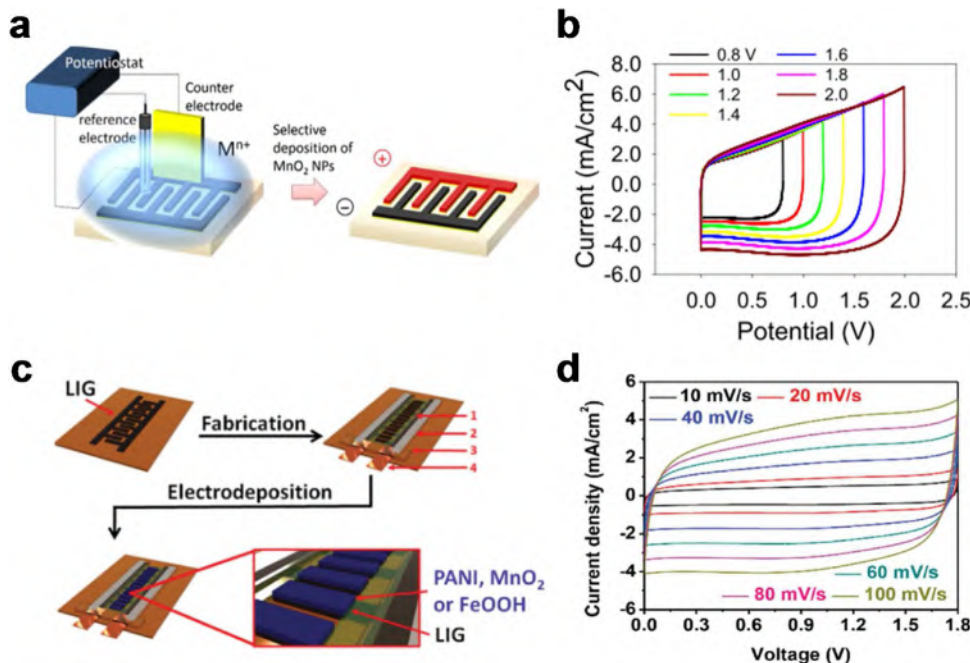


Fig. 6. LDG-based asymmetric micro-supercapacitors. (a) Selective electrodeposition of MnO₂ nanoparticles on an LSG scaffold. (b) Progressive cyclic voltammograms illustrating the 2 V voltage window of LSG/MnO₂//LSG device. Adapted with permission from reference [66]. Copyright 2014, National Academy of Sciences. (c) Fabrication of all-pseudocapacitive micro-supercapacitor by selective electrodeposition of electroactive materials. (d) Cyclic voltammograms of the asymmetric MSC (voltage window of 1.8 V) at different scan rates. Adapted with permission from reference [116]. Copyright 2015, Wiley-VCH.

window. One approach to achieve this is through the asymmetric design of electrodes [115,116]. In this type of device, the complementary potential windows of positive and negative electrode materials add up to increase the operating voltage. Since the energy density of the device is determined by its capacitance and the square of the working voltage ($E=CV^2/2$), the effect of enlarging the voltage window is significant. The fabrication of asymmetric micro-supercapacitors by conventional photolithography involves at least a two-step lithography process and the use of a special photomask. However, LDG patterns enable direct and selective deposition of the right choice of materials in designing asymmetric MSCs in a single step.

El-Kady et al. demonstrated the scalable fabrication of graphene-based asymmetric micro-supercapacitors using “top-down” LightScribe lithography and “bottom-up” selective electrodeposition. Positive LSG-MnO₂ and negative LSG electrodes were employed in designing an asymmetric 3D micro-supercapacitor (Fig. 6a). As illustrated in Fig. 6b, the LSG-MnO₂//LSG 3D asymmetric micro-supercapacitor operated at a voltage window of 2 V while exhibiting a volumetric stack capacitance of 250 F/cm³, which is higher than state-of-the-art carbon MSCs (<5 F/cm³). The array of compact hybrid LSG-MnO₂ 3D MSCs was integrated with solar cells to demonstrate efficient solar energy harvesting and storage [66].

Li et al. demonstrated the fabrication of all-solid-state, flexible asymmetric MSCs by electrochemical deposition [116]. Pseudocapacitive materials were electrodeposited on the LIG fingers. LIG not only works as an electrical double layer electrode but its conductive nature enabled the electrodeposition of pseudocapacitive materials such as MnO₂, FeOOH, and polyaniline (PANI) to form LIG-MnO₂, LIG-FeOOH, and LIG-PANI composites, respectively (Fig. 6c). An asymmetric MSC was fabricated by employing LIG-FeOOH as a negative electrode and LIG-MnO₂ as a positive electrode (LIG-FeOOH//LIG-MnO₂). When tested in PVA/LiCl electrolyte, the asymmetric device displayed a voltage window of 1.8 V (Fig. 6d). The areal and volumetric capacitance of the full asymmetric device

was estimated to be 21.9 mF/cm² and 5.4 F/cm³ respectively, at a current density of 0.25 mA/cm². These values resulted in areal and volumetric energy/power performance (Maximum $E_A = 9.6 \mu\text{Wh}/\text{cm}^2$ and $E_V = 2.4 \text{ mWh}/\text{cm}^3$; Maximum $P_A = 11564 \mu\text{W}/\text{cm}^2$ and $P_V = 2891 \text{ mW}/\text{cm}^3$), which is superior to symmetric devices.

Moosavifard et al. developed similar asymmetric 3D LGS/CoNi₂S₄//LSG MSCs by laser scribing followed by selective electrodeposition [117]. 3D graphene not only provides current collecting pathways for the electrons but also high surface area support for the direct growth of NiCo₂S₄. These asymmetric devices displayed a stable operating voltage window of 1.7 V, which is higher than the conventional activated carbon symmetric capacitors in aqueous electrolytes (0.8–1 V). Device volumetric stack capacitance up to 112.4 F/cm³ was achieved with an energy density of 49 Wh/L. This is comparable to those of packaged lead-acid battery cells. These studies proved the potential of the 3D conductive LDG platform to develop hybrid electrodes and hybrid on-plastic energy storage devices. Table 2 summarizes the electrochemical performance of various LDG-based supercapacitors in literature [44,51,52,65–67,100,113,114,116–120].

Effect of doping on electrochemical performance

To improve the electrochemical performance of graphene-based materials, various strategies have been employed to tune the electronic band structure. Among them, heteroatom doping including boron, nitrogen, phosphorous and sulfur is known to be an active area of research. For instance, *p*-type doping by boron atoms into the carbon lattice can shift the Fermi level toward the valence band, causing enhancement in charge storage and transfer within the doped graphene structure. Heteroatom doping can also contribute additional pseudocapacitance and thus improve the overall electrode capacitance. Peng et al. demonstrated the direct fabrication of B-doped porous graphene micro-supercapacitors [118]. They incorporated boric acid into polyimide sheets followed by laser-based transformation and patterning simultaneously. Similarly, Guo et al.

Table 2

Summary of LDG-based supercapacitors reported in literature.

Type	Design	Configuration	Electrolyte	Voltage (V)	C _A (mF/cm ²)	C _V (F/cm ³)	E _V (mWh/cm ³)	P _V (W/cm ³)	References
GO→rGO (22 μm)	In-plane	Symmetric	1 M Na ₂ SO ₄ 1 M H ₃ PO ₄	1 1	1.2 3.67	N/A 0.4	1 0.04	100 1	[51]
GO→LSG (68.2 μm)	Sandwich	Symmetric	PVA/H ₃ PO ₄ tetraethylammonium tetrafluoroborate	1 3	N/A 4.82	0.4 N/A	0.04 0.4	1 10	[44]
GO→LSG (7.6 μm)	In-plane	Symmetric	EMIMBF ₄	4	5.02	N/A	1	10	[65]
PI→LIG (25 μm)	In-plane	Symmetric	PVA/H ₂ SO ₄ 1 M H ₂ SO ₄	1 1	2.3 3.5	2.35 1.5	N/A 0.3	200 50	[52]
PI/H ₃ BO ₃ →B doped LIG (25 μm)	In-plane	Symmetric	BMIM-BF ₄ PVA/H ₂ SO ₄	3.5 1	2 16.5	0.8 6	1 0.3	100 1	[118]
GO→LSG+ED (MnO ₂)	In-plane	Asymmetric	1 M Na ₂ SO ₄	0.9	400	250	30	1	[66]
GO/RuCl ₃ →LSG/RuO ₂ (25 μm)	In-plane	Symmetric	1 M H ₂ SO ₄	1	70	158	1	1	[67]
PI→LIG (25 μm)	Sandwich	Symmetric	PVA/H ₂ SO ₄	1	9	N/A	0.2	1	[113]
GO/HAuCl ₄ →rGO/Au Nps (13.7 μm)	In-plane	Asymmetric	PVA/H ₂ SO ₄	1	0.77	17.2	N/A	N/A	[100]
PI→LIG+ED (FeOOH(41 μm)/MnO ₂ (101 μm))	In-plane	Asymmetric	PVA/LiCl	1.8	21.9	5.4	3.2	2.89	[116]
GO→rGO+ED (CoNi ₂ S ₄)	In-plane	Asymmetric	PVA/KOH	1.7	N/A	122.4	49	10	[117]
PI→LIG (80 μm)	In-plane	Symmetric	PVA/H ₂ SO ₄	1	22.4	2.8	N/A	N/A	[119]
PI→LIG	In-plane	Symmetric	PVA/H ₂ SO ₄	1	10	N/A	N/A	N/A	[120]
Lignin→LIG	In-plane	Symmetric	PVA/H ₂ SO ₄	1	25.1	6.27	1	2	[114]

GO: graphene oxide; PI: polyimide; PVA: polyvinyl alcohol; LSG: laser-scribed graphene; LIG: laser-induced graphene; ED: electrodeposition.

prepared reduced GO with 10 wt% of nitrogen doping by using femtosecond laser irradiation [121]. Recently, Fu et al. achieved 8 wt% of nitrogen doping by using CO₂ laser reduction of graphite oxide containing nitrogen-rich carbon nanoparticles [122]. These approaches are based on simultaneous reduction and doping of GO and showed improvement in electrochemical performance when compared to undoped graphene electrodes.

As illustrated in Fig. 7, Peng et al. employed boric acid mixed polyamic acid solutions (solvent: N-methylpyrrolidone) as a PI precursor film. Different weight percentages of boric acid (H₃BO₃), 1–8 wt% relative to PAA, were mixed and bath sonicated for 30 min to form a uniform precursor solution [118]. Condensation of the precursor solution produced a boric acid-containing polyimide. The laser transformed H₃BO₃-PI into B-LIG patterns, as illustrated in Fig. 7a. The preference of boric acid over other boron precursors is based on the ease of dehydration and polymerization upon thermal treatment.

The electrochemical performance of B-LIG with different initial H₃BO₃ loadings was compared. PVA/H₂SO₄ gel electrolyte was coated onto the interdigitated electrodes with Kapton tape sealing to avoid touching the Ag paint at the edges for contact purposes (Fig. 7b). Among all the devices, 5B-LIG-MSC exhibited higher current values in CV curves at the same scan rate, confirming the highest areal capacitance (Fig. 7c). The increase of boron doping from 0 to 5 wt% raised the areal capacitance by four times compared to undoped LIG. They hypothesized that the optimal boron doping in LIG improves the capacitance by increasing the hole charge density and thus enhances the charge storage. The areal capacitance of corresponding devices reached up to 16.5 mF/cm², which is three times higher than undoped LIG devices, with concomitant energy density increasing by 5–10 times. However, higher levels of boron doping beyond 5 wt% might induce more scattering sites for the electrons in the LIG sheets, causing the diminished conductivity values and thus diminished capacitance.

The effect of nitrogen doping into LDG electrodes on the electrochemical storage of Na-ions was recently investigated. Bulk graphite has been widely employed as a stable and robust anode material for commercial Li-ion battery technology today [123]. However, graphite cannot intercalate large Na-ions, posing a challenge in developing robust and high capacity Na-ion anodes. Hard

carbon composed of nanodomains of graphene layers showed promise as a reversible Na-ion anode but suffered from the limitations of Na-plating issues at higher current densities. As such, the trend toward developing conductive carbon anode materials is highly desired for high rate Na-ion storage. Developing open architectures of graphitic materials with expanded structures in a self-standing manner are important for stable and high rate electrochemical storage of Na-ions.

Zhang et al. employed a novel strategy based on the single-step laser-induced transformation of urea-containing polyimide into an expanded 3D graphene anode, with simultaneous doping of high concentrations of nitrogen (13 at%) [124]. The versatile nature of this laser process enabled direct bonding of the 3D graphene anode to the current collectors without the need for binders or conductive additives. This presents a clear advantage over chemical or hydrothermal methods (Fig. 8a). A very thin layer of PI (which need not be continuous) could act as a glue that improves adhesion of LDG to Cu surface. The ohmic contact between the Cu and graphitic material can be confirmed from the electrochemical response, where interfacial impedance between the two can be measured. By optimizing the laser parameters and surface pre-treatments of Cu and Ni foams, it is possible to grow graphitic carbon from polyimide precursors coated on those substrates. Since carbon has high solubility in Ni matrix, it is expected that graphitic carbon growth on Ni foam substrates may be feasible as well. Such strategy can be used to fabricate 3D porous graphitic electrodes for a variety of electrochemical applications. This study compared the electrochemical storage of Na-ions of LSG electrodes: (i) LSG without nitrogen doping (LSG), (ii) nitrogen doping in the air (NLSG-1) and (iii) nitrogen doping in a nitrogen environment (NLSG-2). The NLSG-2 electrode exhibited an initial coulombic efficiency (CE) up to 74% (Fig. 8b), which exceeds that of most reported carbonaceous anodes, such as hard and soft carbon [124]. In addition, Na-ion capacities up to 425 mAh g⁻¹ at 0.1 A g⁻¹ were achieved with excellent rate capabilities. A capacity of 148 mAh g⁻¹ at a current density of 10 A g⁻¹ was also obtained with excellent cycling stability (Fig. 8c). These results open a new path for the fabrication of high-performance 3D graphitic anodes directly on current collectors for Na-ion battery anodes that can be optimized to work as well for K-, Mg and Al-batteries. The ability to tune up the electrochemical properties of

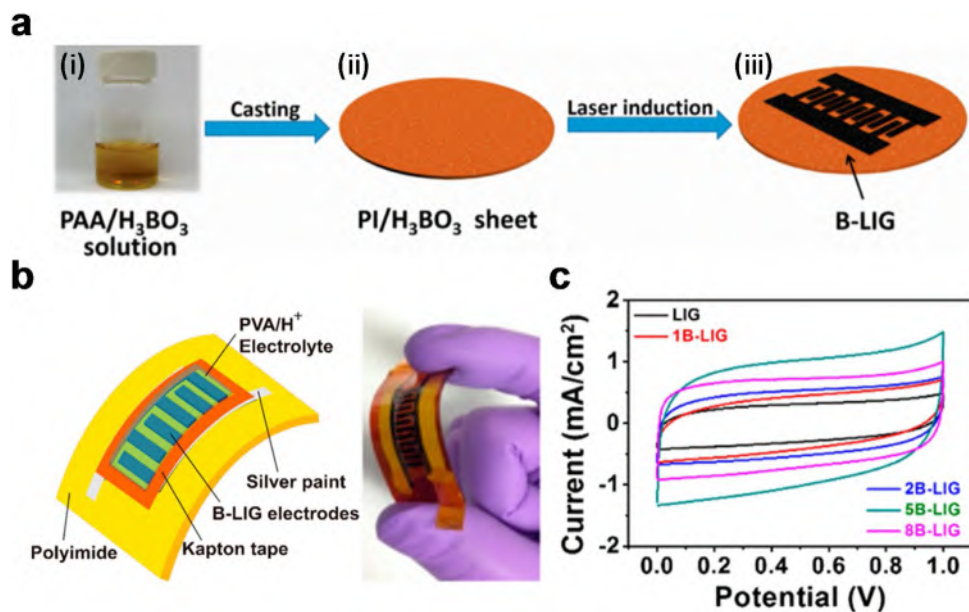


Fig. 7. Fabrication of B-doped LIG micro-supercapacitors (B-LIG-MSC). (a) (i) Mixing of polyamic acid with H_3BO_3 solution, (ii) condensing into $\text{PI}/\text{H}_3\text{BO}_3$ sheet, (iii) laser-induced transformation into boron-doped porous graphene patterns. (b) Flexible solid-state B-LIG micro-supercapacitor in gel electrolyte. (c) Comparing the electrochemical performance of LIG micro-supercapacitors with different amounts of boron loadings. Adapted with permission from reference [118]. Copyright 2015, American Chemical Society.

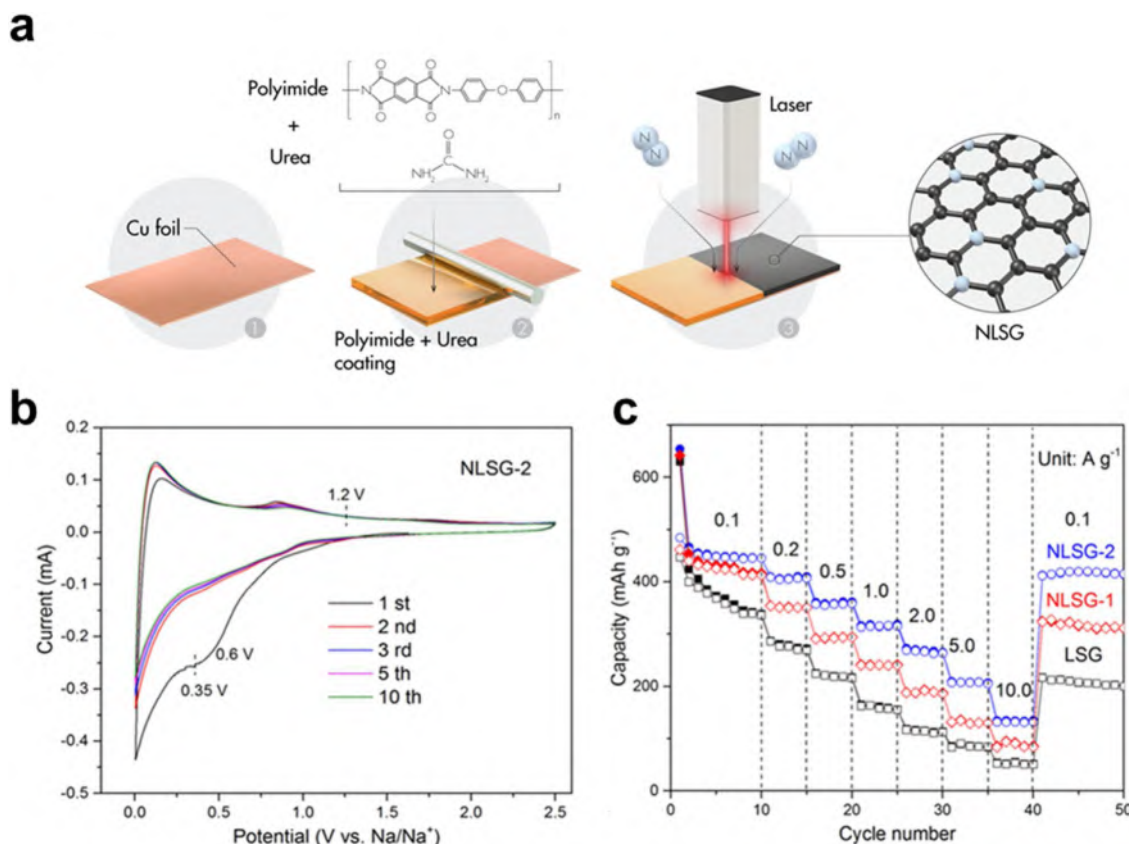


Fig. 8. (a) Schematic illustrating the process flow used to fabricate the nitrogen-doped 3D graphene directly onto Cu foil through laser irradiation. (b) CV curves of NLSG-2 electrodes (at 0.1 mV s^{-1}). (c) Rate performance of LSG, NLSG-1 and NLSG-2 electrodes at different current densities. LSG: laser-scribed graphene from polyimide. NLSG-1: Urea containing PI; LSG is formed in the air. NLSG-2: Urea containing PI; LSG was formed under a nitrogen environment. Adapted with permission from reference [124]. Copyright 2018, Wiley-VCH.

LDG electrodes through doping strategies is compelling. Such doping strategies could lead to exploring high rate LDG-based energy storage devices. Since LDG electrodes offer higher electrochemi-

cal surface area for metal ions adsorption/insertion compared to restacked layered materials, they are better electrodes for capacitive storage applications. LDG electrodes should also be explored

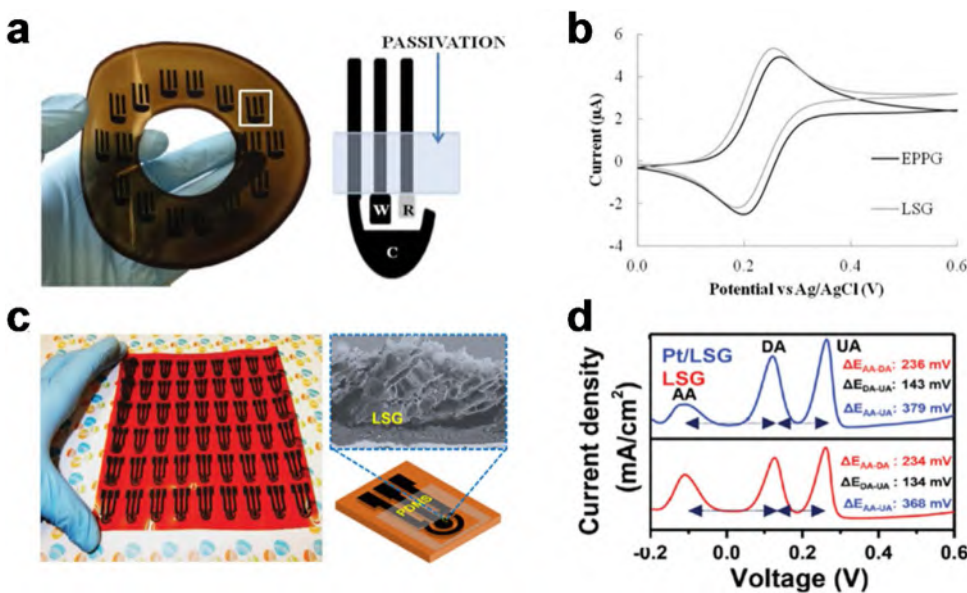


Fig. 9. (a) Three-electrode patterned LSG (from GO) electrodes. (b) Cyclic voltammograms of 1, 1'-ferrocene methanol at a scan rate of 10 mV s^{-1} at EPPG electrode surfaces compared to the LSG system. Adapted with permission from reference [137]. Copyright 2014, Royal Society of Chemistry. (c) Digital photograph showing scalable fabrication of LSG (from PI) electrode arrays (the projection displays the scheme of a single 3-electrode pattern on the PI sheet and a cross-sectional SEM micrograph of LSG). (d) Differential pulse voltammetry scans of LSG and Pt/LSG electrodes (vs. Ag/AgCl) in 0.1 M PBS (pH 7.0) containing $1 \times 10^{-3} \text{ M AA} + 40 \times 10^{-6} \text{ M DA} + 40 \times 10^{-6} \text{ M UA}$. Adapted with permission from reference [73]. Copyright 2015, Wiley.

for electrochemical storage of different metal cations. Further, laser parameters should be optimized to produce porous carbon type cathode materials for metal adsorption. Hence, we expect that laser processing can be a promising route for the fabrication of in-plane metal-ion capacitors via optimized laser conditions [125].

On-chip biosensors

Electrochemical sensing has long been recognized as a promising technique for the detection of biologically significant molecules, but stringent demands exist on sensor performance. These include high sensitivity, selectivity, fast response besides fairly low cost fabrication [126]. Carbon electrodes have become attractive for this type of sensor applications due to their electronic conductivity, chemical robustness in electrolyte media and efficient charge transfer for a wide variety of analytes [127]. Due to its 2D morphology, graphene has been a favored platform for electrochemical sensing applications. The key concepts of the electron transfer rate and analytical performance in graphene-based sensors are governed by the combined effects of the specific surface area, electronic conductivity and available edge plane sites [128–130].

Heterogeneous electron transfer rates

Graphene-based electrochemical sensing platforms often employ chemically made graphite oxide that is subsequently reduced by chemical, electrochemical, thermal or hydrothermal routes [131–135]. However, electrodes processed through the above methods tend to be difficult for integration as practical devices. This is due to the requirement of additives, fillers and polymeric binders for coatings. This introduces many drawbacks, such as the reduction of the specific surface area, electronic conductivity and charge transfer rate due to the inherent layer restacking nature of graphene during the solution processing [136]. Therefore, fabricating graphene-based devices while getting rid of the above detrimental effects is highly important for electrochemical sensing applications. The first step in this direction was developed by the Kaner group, who designed a graphene

sensor prototype on GO film by laser scribing (Fig. 9a) [137]. The LSG electrode demonstrated a fast heterogeneous electron transfer rate (k°) of $0.02373 \text{ cm s}^{-1}$ for the potassium ferricyanide, $\text{K}_3[\text{Fe}(\text{CN})_6]$ redox mediator. This exceeds the highly relevant carbon alternatives such as edge plane pyrolytic graphite, EPPG ($k^{\circ} = 0.022 \text{ cm s}^{-1}$), and basal plane pyrolytic graphite, BPPG ($k^{\circ} = 10^{-9} \text{ cm s}^{-1}$) [138,139]. This stand-alone prototype displayed intrinsic electrochemical properties without the summative effects in the case of powdery electrodes (Fig. 9b). This technique offers free-standing 3D graphene electrode architecture while avoiding the external binders and additives – a new step away from the conventional powdery electrodes. However, as mentioned, the preparation protocol involves a multi-step technique involving the preparation of GO, casting of GO on a DVD drive and finally scribing with LightScribe technology. The quality of graphene produced is thus highly dependent on the quality of GO (mainly due to oxygen functionalities in LSG, which influences electrochemical behavior) and cannot be controlled by an external laser source (here a LightScribe DVD drive).

The issues caused by the complicated multi-step fabrication procedure were avoided by the single-step fabrication of a sensor prototype by direct laser-induced transformation of a PI sheet under ambient atmosphere (Fig. 9c, d) [73]. These electrodes displayed a fast HET rate (k°) of 0.1150 and 0.0868 cms^{-1} for both inner-sphere and outer-sphere redox mediators, $[\text{Fe}(\text{CN})_6]^{4-}$ and $[\text{Ru}(\text{NH}_3)_6]^{3+}$ respectively, which is significantly better than other types of graphene-based platforms. The k° value was further enhanced by selective anchoring of Pt nanoparticles over LSG and is comparable to many other graphenes obtained through different routes and commercial pyrolytic graphite-based electrodes (illustrated in Table 3) [73,137–141]. These PI-derived LSG electrodes exhibit significantly improved electrocatalytic activity in the oxidation of ascorbic acid (AA), dopamine (DA) and uric acid (UA) with enlarged peak separations ($\Delta E_{\text{AA-DA}} = 234$ and 236 mV , $\Delta E_{\text{DA-UA}} = 134$ and 143 mV and $\Delta E_{\text{AA-UA}} = 368$ and 379 mV) for LSG and Pt/LSG respectively. The detection of these biomarkers was consequently achieved with high sensitivity and selectivity in a wide concentration range. This is ascribed to the binder-free 3D porous network of

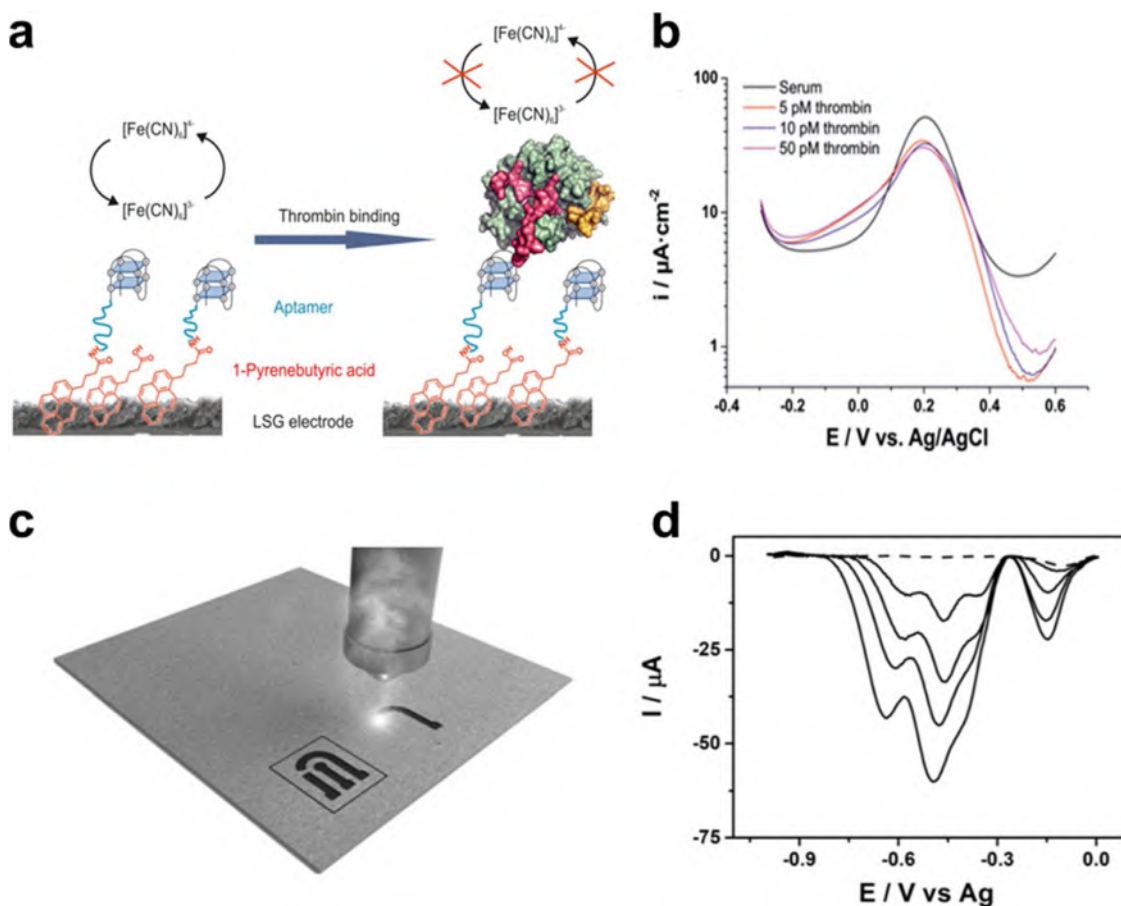


Fig. 10. (a) Schematic depicting electrochemical thrombin detection mechanism using LSG. (b) Change of the DPV peak current at varying thrombin concentration in serum. Adapted with permission from reference [143]. Copyright 2017, American Chemical Society. (c) Laser fabrication of paper-based analytical devices. (d) Picric acid detection using differential pulse voltammograms with the presence of 0.48, 0.91, 1.30, and 2.0 mmol L⁻¹ picric acid (solid curves) and 0.1 mol L⁻¹ PBS (pH 2.0). Adapted with permission from reference [144]. Copyright 2017, Wiley.

Table 3
HET rate (k^*) of two redox mediators using different graphitic electrode materials.

Electrode	k^* (cm/s)		References
	$[Fe(CN)_6]^{4-}$	$[Ru(NH_3)_6]^{3+}$	
Pt/LSG	0.28230.1150	0.23120.0868	[73]
BPPG	10^{-9} 0.022	0.00380.00877	[138,139]
L-graphene	0.02373	—	[137]
CVD-Gr	0.014	0.012	[141]
Q-graphene	0.0186	0.0177	[140]
q-graphenem-graphene	—	0.001580.0011	[138]

Pt/LSG: Pt nanoparticles decorated laser-scribed graphene; LSG: laser-scribed graphene; BPPG: basal plane pyrolytic graphite; EPPG: edge plane pyrolytic graphite; L-graphene: laser-induced graphene from GO; CVD-Gr: graphene grown on copper foil by chemical vapor deposition; Q-graphene: polyhedral structure graphene; q-graphene: few-layer (termed quasi-) graphene grown via CVD; m-graphene: mono-layer graphene grown via CVD.

LSG with numerous edge plane sites and plenty of available electrochemical active surface area.

Electrochemical biosensing

An important aspect of using the graphene-based platform in electrochemical bio-sensing is its effective immobilization of bio-enzymes [142]. Many of the sensing platforms, including the commercialized glucometers, are based on enzymatic reactions with bio-analytes. In this regard, graphene offers a 2D conductive plane with the high surface area to hold enzymes and simultaneously provide conducting paths for the electrons generated during the biochemical reactions. However, the critical issues in real graphene device fabrication are the requirement of the binder

and the restacking of layers, which leads to decreased surface area due to the inherent nature of graphene and consequently influences the detection limit of bioanalytes. The 3D LSG scaffold may be a better choice to circumvent the above issues. Anchoring 1-pyrenebutyric acid to LSG followed by the covalent attachment of an aptamer in LSG-based biosensor displayed extremely low detection limits of thrombin at a concentration of 1 pM in the buffer and 5 pM in the complex matrix of serum (Fig. 10a, b) [143].

Araujo et al. demonstrated laser scribing fabrication of electrochemical paper-based analytical devices by pyrolyzing the surface of paperboard as shown in Fig. 10c [144]. This is a single step fabrication of non-graphitizing carbon material with aluminosilicate nanoparticles and this composite material was employed in detecting ascorbic acid and caffeic acid (important antioxidants

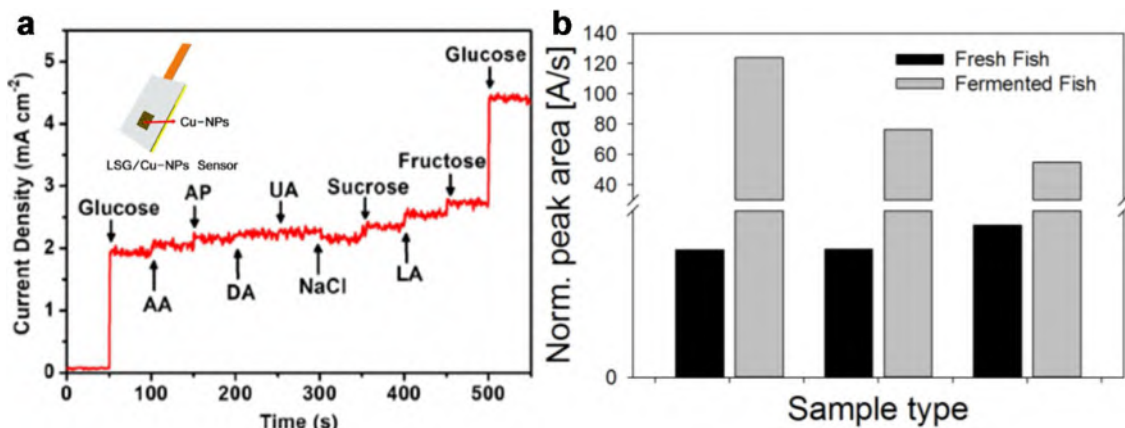


Fig. 11. (a) Nonenzymatic glucose sensor fabrication by electrodeposition of Cu nanoparticles on LSG platform (inset), interference test of the LSG/Cu-NPs sensor in 0.1 M NaOH solution containing the 1 mM of glucose and the 0.1 mM of interfering species. Adapted with permission from reference [145]. Copyright 2017, Elsevier. (b) Detection of biogenic enzymes from food samples by Cu sensitized LSG sensors towards food safety, normalized peak area used to calculate total BA content from the 3 successive injections of supernatant from non-fermented and fermented fish paste. Adapted with permission from reference [148]. Copyright 2018, MDPI.

present in food). These prototype electrochemical sensors were used for electrochemical sensing of picric acid using differential pulse voltammetry with improved sensitivity in the concentration range of 0.48–2.0 mM (Fig. 10d). Such kind of cost-effective fabrication of paper-based analytical devices may be suitable for a variety of applications including clinical and forensic fields.

Nonenzymatic glucose detection

Implantable glucose biosensors are emerging as they can offer continuous monitoring of blood glucose of diabetic patients. LDG may be a right choice of platform as it offers high electronic conductivity beside having a high electrochemically active surface area. Lin et al., developed nonenzymatic glucose sensor based on LSG platform [145]. Catalytic behavior of electrodeposited Cu nanoparticles was exploited towards glucose oxidation while exhibiting linear detection range from 1 μ M to 4.54 mM at a high sensitivity of 1.518 mA mM⁻¹ cm⁻² and low limit of detection of 0.35 μ M. Further, they demonstrated the selective detection of glucose in the presence of other interfering species in the blood including dopamine, uric acid, sucrose, fructose, and lactose. The anti-interference property of the developed glucose sensor was certified by successive injection of 1 mM of glucose and 100 μ M of interfering species (Fig. 11a). Negligible current response from the other species in contrast to glucose current response makes the developed sensor highly selective to the glucose detection.

Similarly, Bavarian et al. demonstrated a novel and highly sensitive disposable non-enzymatic glucose sensor strip using a direct laser engraved graphene (DLEG) decorated with copper nanocubes [146]. The prototype glucose sensor displayed excellent selectivity, sensitivity (4,532.2 μ A/mM.cm²), low detection limit (250 nM), high reproducibility (96.8%), stability (97.4%) and a suitable linear range of 25 μ M - 4 mM. Zhang et al. reported a new approach for the scalable construction of LIG patterns on diverse substrates by using phenolic resin (PR) as the precursor [147]. The fabricated electrochemical glucose biosensors exhibited a good linear relationship between the concentrations of glucose ranging from 0.2 to 10 mM.

LSG biosensors were also employed for the detection of biogenic amines, which are produced as a result of microbial metabolism of food products. Reagent-free food safety biosensor was fabricated by functionalizing graphene platform with copper microparticles and diamine oxidase [148]. Such kind of biosensors showed an average histamine sensitivity of 23.3 μ A/mM, a lower detection limit of 11.6 μ M, and a response time of 7.3 s. Further, the selectivity of LSG biosensor towards the level of BA concentration was analyzed by

testing fish paste before and after solid-state fermentation with lactic acid bacteria (Fig. 11b). This was analyzed by normalizing the peak area for the fermented and fresh samples and calculated BA levels in the fermented sample were 19.24 ± 8.21 histamine/kg fish paste. Low-cost and rapid fabrication of LSG biosensors can be useful for biogenic amine estimation from a variety of food samples, may serve as an indicator for food safety and quality.

pH sensors

Rahimi et al. demonstrated the fabrication of a highly stretchable electrochemical pH sensor based on conductive polyaniline/LIG composite (see Fig. 12a-f). The CO₂ laser was employed to pyrolyze PI sheet to fabricate graphitic interconnects followed by machining of PI sheet. The porous conductive graphitic carbon was modified by polyaniline as a pH-sensitive electrode. Polyaniline played multiple roles as the conductive filler, binding material, and pH-sensitive membrane. As shown in Fig. 12 g, the pH sensor was tested through the unit change in the pH value (from 4 to 10) and it exhibited distinct potential change at each pH level with an average response time of 58 s. The pH sensor displayed a linear sensitivity of -53 mV/pH with a correlation coefficient of $r^2 = 0.976$ (Fig. 12h). The excellent stability under 100% longitudinal strain in different pH solutions may be useful in developing future wearable point-of-care applications [149].

LIG patterns were employed as sensors for monitoring the quality of water through the detection of unwanted pollutants. For instance, Alahi et al., measured the concentration of nitrate-N present in the water using graphene sensors [150]. They used electrochemical impedance spectroscopy (EIS) to characterize the developed graphene sensors to monitor the quality of water in real time (1–70 ppm) and test the salinity. Cheng et al. demonstrated LIG based sensors for atto- to femtomolar level detection of bisphenol A (BPA) [151]. They immobilized BPA-specific aptamer onto LIG surface as the probe, and its binding with BPA at the electrode was detected by capacitive sensing. Like other methods, such as capacitive sensing methods for detecting Bisphenol A, salinity testing explores the multi-dimensional sensing asset of LIG platforms [151,152].

Electrocatalysis

Due to the limited availability of fossil fuels and adverse environmental issues regarding consumption, many efforts have recently been made on critical renewable energy technologies such as

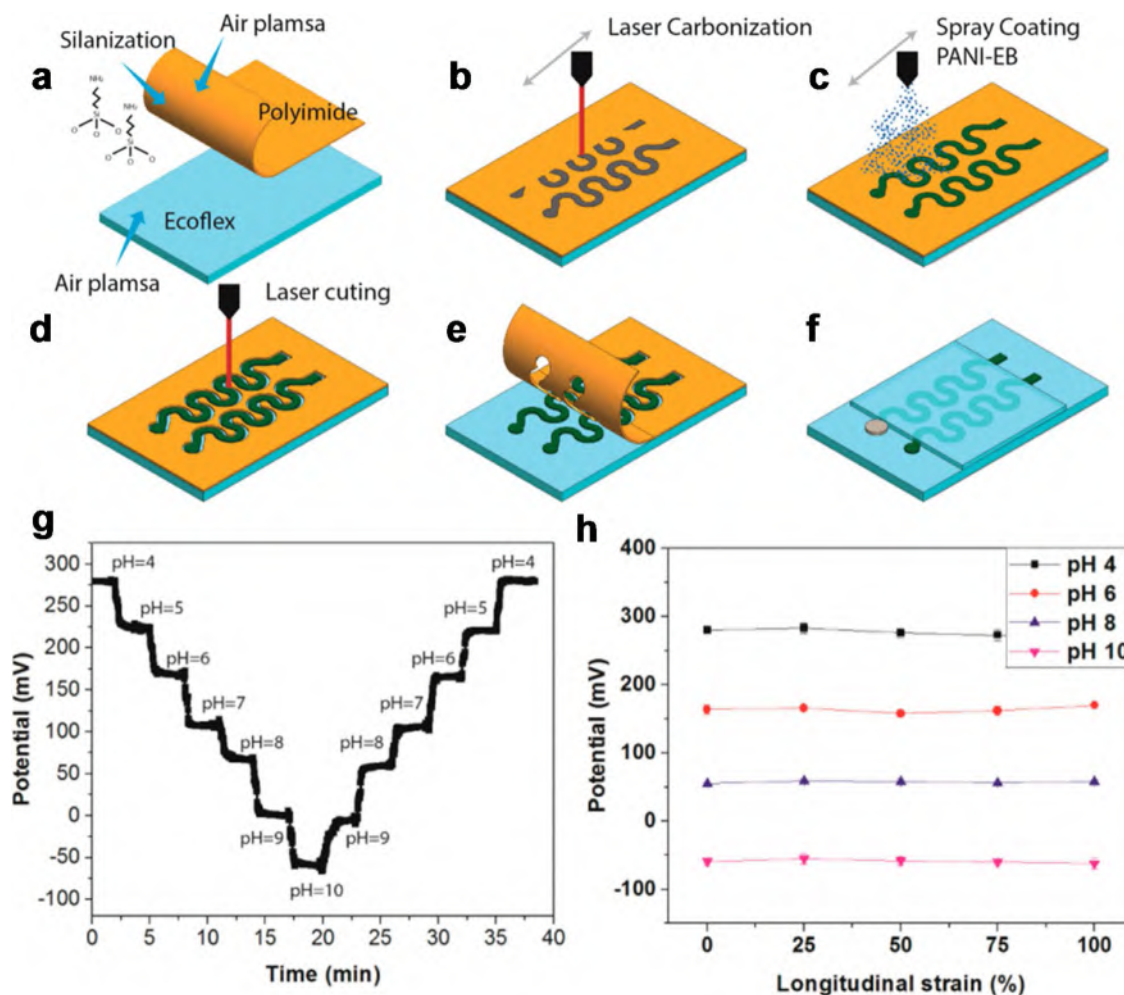
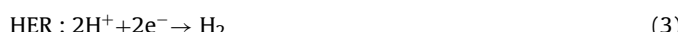


Fig. 12. Fabrication of stretchable pH sensors. (a) Bonding of polyimide to the Ecoflex through silane treatment. (b) serpentine carbon patterns by laser irradiation, (c) spray coated polyaniline onto porous conductive carbon. (d) Machining of polyimide sheet. (e) Removal of excess of polyaniline. (f) Encapsulation of interconnects by another Ecoflex layer followed by the deposition of Ag/AgCl and solid electrolyte. (g) Dynamic pH response of the pH sensor to the unit decrease and increase of pH. (h) Potentiometric responses of a pH sensor to various longitudinal strains in different pH buffer solutions. Adapted with permission from reference [149]. Copyright 2017, American Chemical Society.

fuel cells, batteries, and electrochemical water splitting. The basic reactions for these energy alternatives include oxygen reduction reaction (ORR), oxygen evolution reaction (OER) and hydrogen evolution reaction (HER)



These reactions require efficient catalysts to accelerate reaction kinetics for the feasible electrolyzer. To this end, noble metals, transition metal chalcogenides, carbides, phosphides, and oxides have been studied as efficient electrocatalysts for both HER and ORR [153–156]. However, the use of these catalysts as sole electrodes invites many issues, such as particle agglomeration and prohibitive cost (for noble metals) and the moderate electronic conductivity of transition metal dichalcogenides (TMDs) [157,158]. Developing technology that will markedly minimize noble metal usage while preventing agglomeration with increased electronic conductivity and effective utilization of the catalyst is critical for the future ‘hydrogen economy’. One strategy could be the direct employment of a minimal amount of the catalyst on a self-supported high surface area conductive carbon with effective utilization [159].

Oxygen reduction/evolution reaction catalysts

LDG can meet these requirements as a 3D scaffold for loading catalysts in addition to offering mechanical and conductive support. Ye et al. employed direct laser scribing of metal complex-containing polyimide for in-situ formation of metal oxide nanocrystals into graphitic architecture [160]. They illustrated the generality of this approach by employing Co-, Mo- and Fe-based metal complexes that subsequently transformed into metal oxides with the simultaneous transformation of polyimide into the graphitic scaffold (Fig. 13a). Furthermore, they demonstrated the ORR electrocatalytic activity of various metal oxides-LIG and analyzed using Tafel slopes (Fig. 13b). Among the three types of composites, 5Fe-LIG-A has a Tafel slope of 102 mV/decade, which revealed lower ORR activity compared to 5Co-LIG-A and 5Mo-LIG-A. This study demonstrated that controlled doping and tunable metal oxide structures bonded to LIG as a direct strategy for designing advanced and efficient electrocatalysts.

Zhang et al. demonstrated that oxidized LIG is an efficient electrocatalyst for OER and ORR [161]. The oxygen plasma-treated LIG surface exhibited increased activity in the oxygen reduction reaction. This was attributed to the enhanced adsorption of OER intermediates. It was further suggested that LIG-O could be a promising metal-free catalyst for water splitting and metal-air/O₂

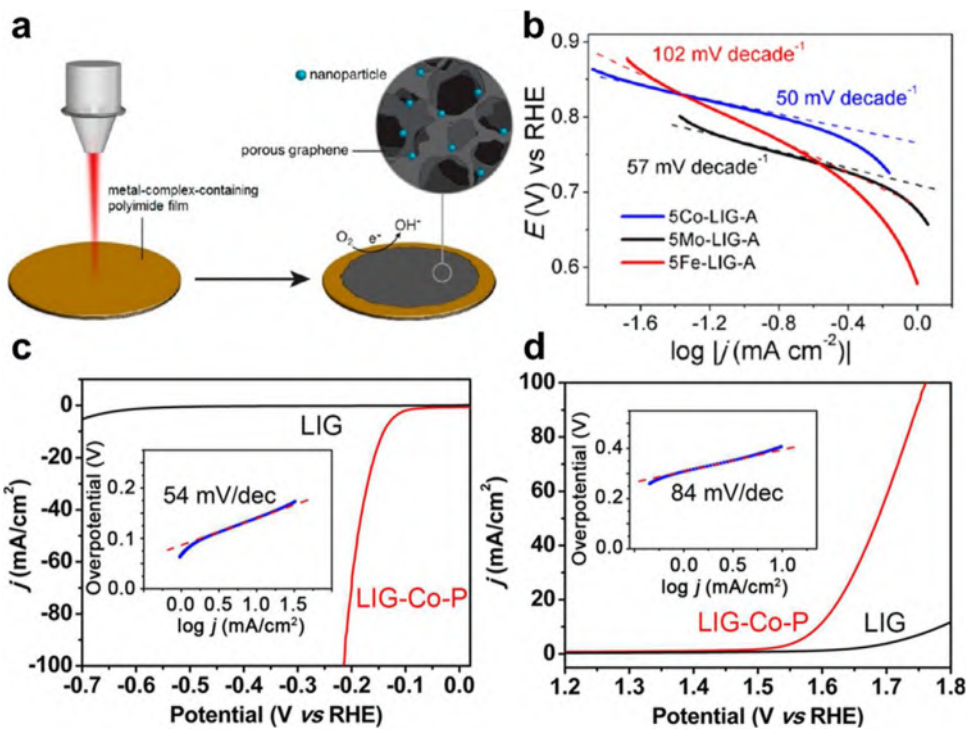


Fig. 13. (a) Formation of Mo-LIG by laser induction on MC-PI film. (b) Tafel plots of 5Co-LIG-A, 5Mo-LIG-A, and 5Fe-LIG-A, derived by mass-transport correction of corresponding RDE data. Adapted with permission from reference [160]. Copyright 2015, American Chemical Society. The LSV profiles of the LIG-Co-P for (c) HER and d) OER in comparison with bare LIG. Corresponding Tafel plots are shown in the insets. Adapted with permission from reference [162]. Copyright 2017, American Chemical Society.

Table 4
Comparison of HER, OER and ORR performance of various LDG-based electrodes.

HER electrode material	Onset potential (V) at $J = -10 \text{ mA/cm}^2$	Tafel slope (mV/dec)	References
Pt/LSG ₂₀₀ (HER)	-0.131	72	[70]
Laser-induced MoS ₂ /carbon hybrids (HER)	-0.216	64	[157]
Pt-LIG (HER)	-0.109	83	
Co-P-LIG (HER)	-0.141	54	
Co-P-LIG (OER)	+0.364	84	[162]
NiFe-LIG (OER)	+0.292	49	
5Co-LIG-A (ORR)	-	50	
5Mo-LIG-A (ORR)	-	57	[160]
5Fe-LIG-(ORR)	-	102	

batteries. Pre-doped Pt-complex into PI was transformed into LIG-Pt under laser irradiation in the H₂/Ar atmosphere. Similarly, after the formation of LIG, catalysts such as NiFe and Co-P layers were electrodeposited on conductive LIG [162]. LIG-Co-P exhibits bifunctional catalytic activity, causing both HER and OER activities in an alkaline medium (Fig. 13 c,d). As expected, LIG displayed no catalytic activity, which is evident from the LSV profiles (the black curves in Fig. 13c and d). Catalytic LIG scaffolds thus offer a practical solution for electrochemical water splitting and can likely be used to construct devices for CO₂ reduction and ORR. Furthermore, the integration of LIG electrodes produces a full device for splitting water into H₂ and O₂. Table 4 displays a comparison of HER, OER and ORR performance of various LDG-based electrodes. This is the reported literature on using LDG as a support for various catalysts in water splitting to date. Given the versatile nature of graphitic electrodes, more efforts are necessary to design competent catalyst electrodes for HER, ORR and OER towards creating future energy resources [70,153,160,162].

HER catalysts

Pranati et al. demonstrated the efficient use of Pt electrocatalysts by atomic layer deposition over LSG for HER. Since LSG is porous and conductive, atomic layer deposition (ALD) offered a conformal deposition of Pt catalysts that exhibited excellent HER performance. The HER performance was optimized with respect to loading Pt through a number of ALD cycles. It was observed that the onset potential drops drastically at about 200 ALD cycles, at which point the cathodic current density rose rapidly and approached that of commercial Pt/C. This strategy provides an avenue for minimal yet effective usage of Pt, leading to enhanced HER activity (Fig. 14a,b) [70]. Similarly, LIG showed promise in synthesizing MoS₂/carbon composite structure in a single-step laser irradiation (Fig. 14c) [163]. The precursor solution composed of citric acid-MoS₂ precursors led to the in-situ synthesis of MoS₂ nanoparticles after laser irradiation. The Tafel slope of bulk MoS₂ was compared with hydrothermal and laser-scribed MoS₂/carbon hybrids (Fig. 14 d). The higher HER activity of the laser-scribed MoS₂/carbon hybrid over other MoS₂ samples can be attributed to the intimate contact of MoS₂ nanoparticles to the conductive carbon matrix and MoS₂ NPs with enhanced catalytic sites. Therefore, the laser scribing technique offers the fabrication of desired catalysts or hybrids through pre-designing the precursor solution. This could lead to fabricating micro fuel cells and microcatalytic reactors.

Other exotic applications

In the fabrication of on-chip micro-supercapacitors and electrochemical storage of Na-ions, LDG offers advantages such as tunable morphology, functionality, controllable doping, and composite formation. LDG also supports the binding of a variety of catalytic particles to develop LDG-based catalysts. The following are some exotic applications of LDG electrodes in the fields of bio-medical and electronics.

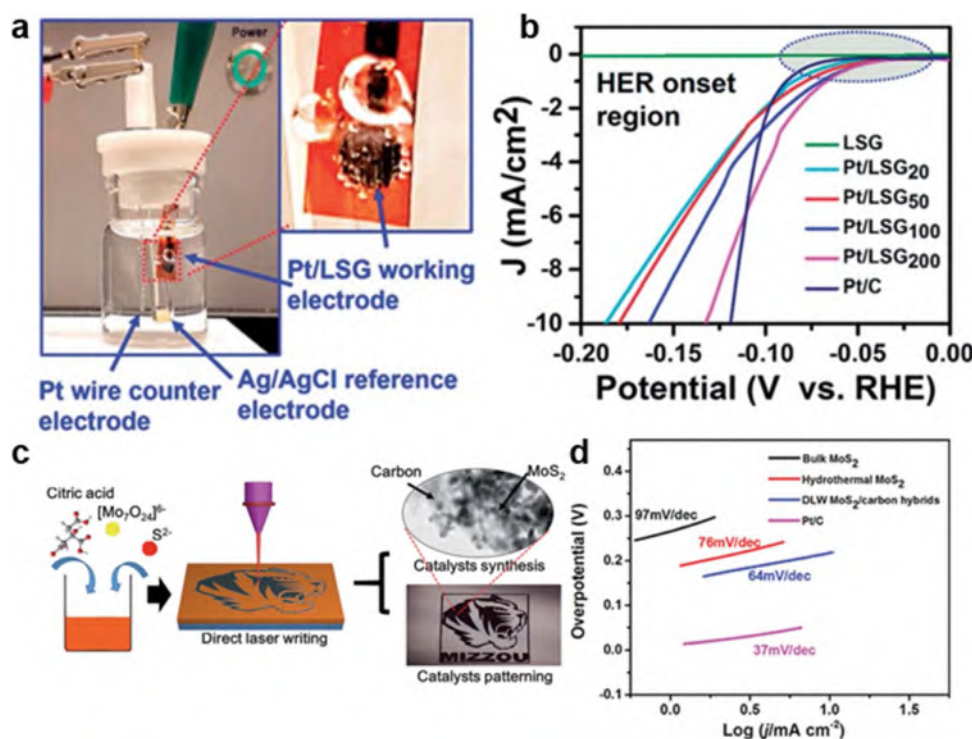


Fig. 14. (a) Digital photograph illustrating a 3-electrode setup comprising of a LSG-based electrode as a working, Pt wire counter and Ag/AgCl as reference electrodes in 0.5 M H_2SO_4 electrolyte. The inset illustrates the instantaneous evolution of H_2 bubbles upon the start of the LSV cycle. (b) LSV displaying HER onset region for LSG and Pt/LSG electrodes compared to commercial Pt/C. Adapted with permission from reference [70]. Copyright 2017, Royal Society of Chemistry. (c) Scheme of the DLW method in fabricating arbitrary patterns composed of MoS_2 /carbon hybrids. (d) Tafel plots of Pt/C, bulk MoS_2 , hydrothermal MoS_2 , and laser-induced MoS_2 /carbon hybrids. Adapted with permission from reference [161]. Copyright 2016, Royal Society of Chemistry.

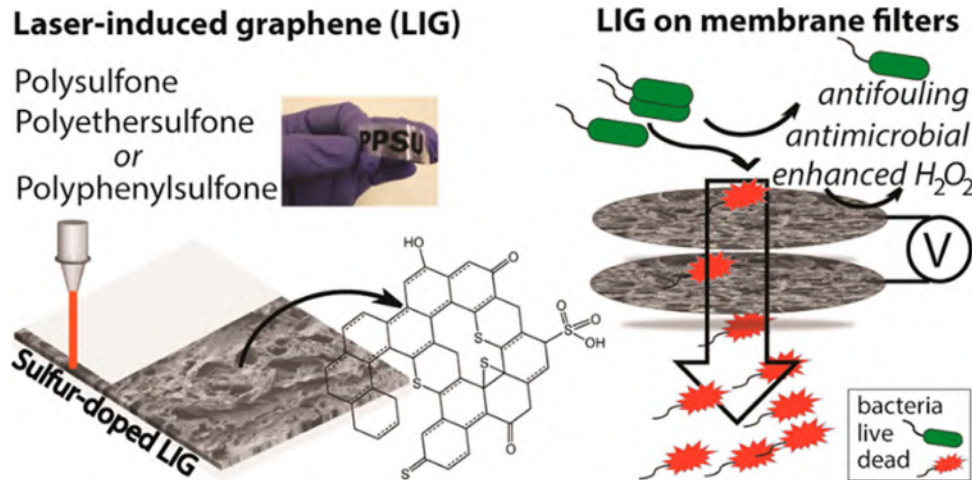


Fig. 15. Sulfur-doped graphene formation on polysulfone membranes through laser induction. Antifouling and antimicrobial properties of sulfur-doped LIG-based PSU membranes. Adapted with permission from reference [71]. Copyright 2018, American Chemical Society.

Antifouling properties

Studies have investigated the antibacterial properties of graphene-based nanomaterials, which stem from its nanosized sharp edges and atomic composition. In this context, LIG offers a scaffold rich in edge plane sites and functionalities. A recent study by Singh et al. demonstrated the antimicrobial and anti-biofilm properties of LIG based on physical and electrical contact of the bacterial cells to the LIG surfaces [71]. This opened new avenues for exploring LIG as a biofouling platform.

Another study by the same group revealed the active microbial killing function of sulfur-doped LIG by transforming the top

layer of polysulfone membranes into LIG through laser irradiation (Fig. 15) [71]. S-doped LIG displayed exceptional biofilm resistance and potent antimicrobial killing effects when treated with *Pseudomonas aeruginosa* and mixed bacterial culture. The hybrid PES-LIG membrane-electrode ensured complete elimination of bacterial viability in the permeate (6-log reduction) in a flow-through filtration mode at a water flux of $\sim 500 \text{ L m}^{-2} \text{ h}^{-1}$ (2.5 V) and at $\sim 22\ 000 \text{ L m}^{-2} \text{ h}^{-1}$ (20 V). The functional PSU-LIG, PES-LIG and PPSU-LIG surfaces have the potential to be incorporated into bio-medical and environmental devices and technologies. This kind of anti-biofilm activity of LIG surfaces and electrodes may be an efficient way to protect surfaces that are susceptible to biofouling in

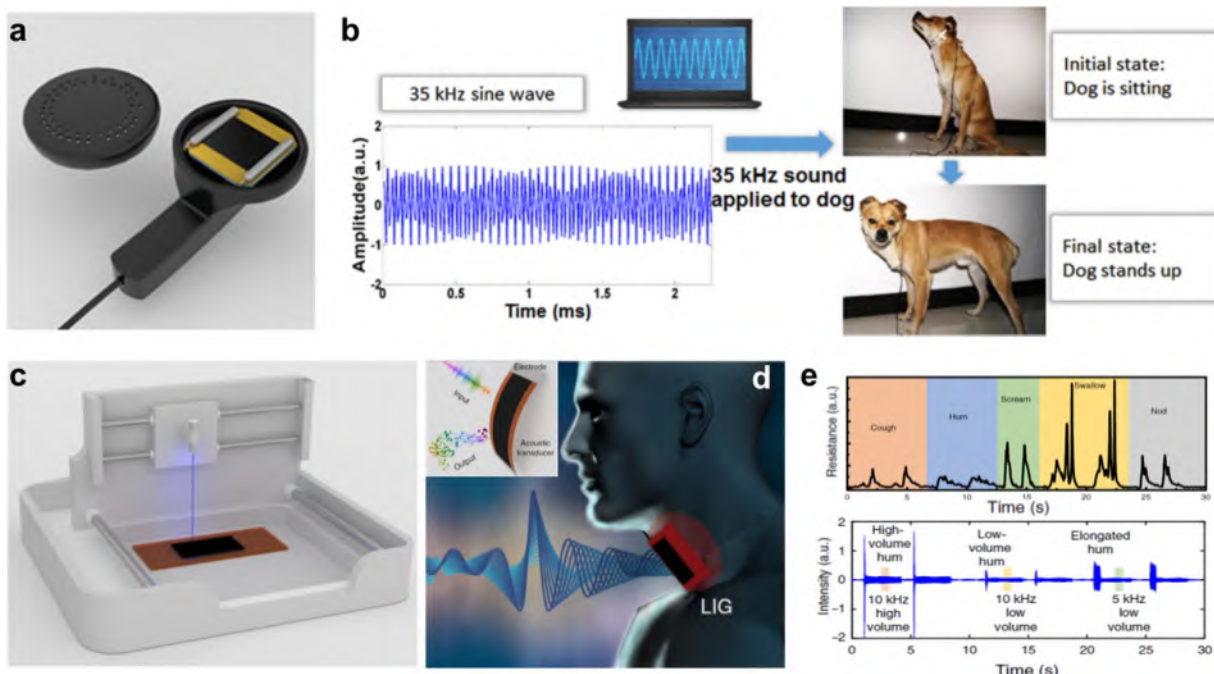


Fig. 16. (a) Graphene earphone in a commercial earphone casing. (b) Training the dog through the earphone. The dog stands up after receiving a familiar 35 kHz signal. (c) One step laser induction of PI to make laser-derived graphene using the blue laser. (d) The artificial throat can detect the movement of the throat and generate controllable sound. Adapted with permission from reference [81]. Copyright 2014, American Chemical Society. (e) Top panel: changes in resistance values with respect to a cough, hum, screaming etc. Bottom panel: High-volume, low-volume and elongated tone hum are detected by the LIG intelligent throat and converted into high-volume 10 kHz, low-volume 10 kHz and low-volume 5 kHz sound, respectively. Adapted with permission from reference [72]. Copyright 2017, Nature Publishing Group.

environmental applications, specifically in water treatment technology. Lu et al. recently employed 3D graphene electrodes for cell alignment and tissue engineering, opening new avenues for flexible graphene patterns for 3D cell or tissue culture to promote tissue engineering and drug testing applications [164].

Electroacoustic applications

LDG can also be suitable for certain electronic applications, although it is not as high quality as the graphene obtained through mechanical exfoliation and high-temperature growth methods. Tian et al. demonstrated the wafer-scale fabrication of graphene earphone units through the laser scribing approach (Fig. 16a) [81]. During the laser scribing process, the rapid expansion of graphene layers resulted in air gaps between layers that can prevent thermal leakage to the substrate. It was revealed that after being tested over a sound frequency ranging from 100 Hz to 50 kHz, the graphene earphone exhibited a reasonably flat frequency response (Fig. 16b). The LSG-based earphone was useful not only for human beings (whose sound frequency range is 20 Hz - 20 kHz) but also for communication with dogs through 35 kHz sound waves.

Tao et al. demonstrated the fabrication of an artificial throat based on LIG on a polyimide substrate [72]. The key characteristics of LIG include high thermal conductivity with low heat capacity and porous morphology. The former is needed to serve as a thermoacoustic sound source; the latter can detect weak vibrations and is suitable for sound detection. Therefore, LIG offers the single-step fabrication of a smart acoustic device that not only generates but also detects sound [72]. The fabrication of an artificial throat is very simple. A rectangular LIG was produced on a PI sheet after irradiating it with a 450 nm laser (Fig. 16c). This kind of LIG pattern integrates the functions of emitting and detecting sounds as illustrated in Fig. 16d. To test the LIG, it was attached to the human throat and simple throat vibrations, including a cough, hum, scream, swallow and nod, were detected by recording the magni-

tude of resistance values (Fig. 16e). These results indicate that a LIG artificial throat can convert unknown sounds into controllable and predesigned sounds. A LIG-based artificial throat may be useful for voice control devices for disabled people.

Luo et al. employed LIG patterns on PI as flexible piezoresistive sensors in probing gesture registration and man-machine interactions [58]. The graphitic sensor gauge factor displayed an exponential dependence on the ratio of the laser power to the scanning speed, which is key in controlling the sensitivity of the graphitic piezoresistive sensor. The optimized device exhibited a high gauge factor of 12. The versatile graphitic sensor can detect finger gestures and heartbeats, indicating that the sensor is sensitive to feeble mechanical motions. Tian et al. also reported a GO-derived LSG-based strain sensor that offered a good linear response to strain and excellent multi-cycle operation [165]. Strong et al. demonstrated the use of interdigitated LSG electrodes as a sensing platform for NO₂ gas. The LSG-based sensor displayed reversible operation while detecting up to 20 ppm of NO₂ gas in the dry air [69].

The highly conductive, porous and flexible nature of LIG and, more importantly, its potential to be patterned into any desired design has attracted a diverse community. For instance, Lin et al. reported the lithography-free monolithic fabrication of a flexible ZnS/SnO₂ ultraviolet photodetector device, in which in-situ LIG-like materials served as lateral electrodes [166]. Such a device is expected to have high mechanical flexibility and excellent optoelectronic performance due to robust interfaces between LIG and ZnS/SnO₂. Graphene achieved a remarkable thermal conductivity enhancement from 0.7 to greater than 1.7 W/m-K by adding polymer, suggesting that this process could be useful for commercial thermal interfacial applications. A comparison of the performance of LDG devices versus graphene produced by other means for a variety of applications is summarized in Table 5 [51,52,58,65,73,83,104,105,118,146,147,165,167–179].

Table 5

Comparison of the performance of LDG versus graphene electrodes produced by other means for a variety of applications.

Devices	Device type and performance metrics				References
Microsupercapacitor	Type	Specific capacitance (mF/cm ²)	Power density (W/cm ³)	Energy density (mWh/cm ³)	
	LDG (4 μm)	4	100	1	[52]
	BLIG	12.4	3	0.56	[118]
	LSG from GO	2.32	200	0.6	[65]
	Graphene *	0.7	0.1	1	[167]
	Activated carbon	11.6	40	10	[104]
	Onion-like carbon (7 μm)	1.7	1000	2	[104]
	Reduced GO (22 μm)	0.51	1.7	0.43	[51]
	CNT arrays (80 μm)	0.428	0.28 mW/cm ²	–	[168]
	Graphene/CNTs (20 μm)	3.93	135	2.42	[169]
	Mesocarbon microbead (100 μm)	100	0.575 mW/cm ²	10 μWh/cm ²	[170]
	Carbide-derived carbon (50 μm)	300	–	–	[105]
Biosensors	Type	Sensitivity (μA/mMcm ²)	Detection potential (mV)	Linearity (μM)	Detection limit (μM)
Dopamine	Pt/LSG	6995.6	–	0.5-56	0.07
	LSG	2259.9	–	0.5-32.5	0.27
	3D graphene ⊥	619.6	0.177	Up to 25	0.025
Glucose	Cu NCs/DLEG	4,532.20	0.55	25-4000	0.25
	LIG ⁿ	–	–	0.2-10000	–
	LSG/Cu-NPs	1518	0.6	1-4540	0.35
	CuO/GO/GC	262.52	0.7	2.79-2030	0.69
	Cu-N-G	48.13	0.5	4-4500	1.3
	CuOG/GCE	1065	0.6	1-8000	1
Other sensors	Type		Patterning method	Gauge factor	
Strain	Total LSG		laser scribe with water lift-off ;	673	[175]
	LSG with pattern		laser scribe	457	[83]
	DLW graphitic lines		Laser scribe on polyimide	112	[58]
	GO derived LSG		Laser scribe on GO film	0.11	[165]
	GO derived graphene micro-ribbons		Laser scribe on GO film	9.49	[165]
	nanographene by CVD		UV-lithography and reactive ion etching	546	[176]
	monolayer graphene by CVD		lithography and plasma etching	151	[177]
	electrochemical exfoliated graphene flakes		stencil printing	1037	[178]
	reduced graphene oxide		vinyl mask	261.2	[179]

BLIG: Boron-Doped Laser-Induced Graphene.

* Inkjet printed graphene micro supercapacitor devices with electrochemically exfoliated graphene.

† RGO prepared by laser reduction and patterning of hydrated graphite oxide films.

⊥3D graphene: Free standing 3D graphene foam.

Cu NCs/DLEG: direct laser engraved graphene (DLEG) decorated with pulse deposited copper nanocubes (CuNCs).

LSG/Cu-NPs: electrodeposited copper nanoparticles on DVD-laser scribed graphene substrate; LIGⁿ: laser-induced graphene (LIG) patterns on diverse substrates by using phenolic resin (PR) as the precursor.

Cu-N-G: Copper nanoparticles (NPs) decorated nitrogen-doped graphene (Cu-N-G).

CuO/graphene (CuOG)-modified glassy carbon (GC) electrode.

DLW graphitic lines: Direct laser write generated graphitic lines; graphene strain sensor (10 mm 10 mm square) graphene micro-ribbons (20 mm width, 0.6 mm long).

Outlook and perspectives

Processing graphene-based materials by conventional ink-jet, screen printing, and roll coating techniques often involve the use of solvents and additional binders. Though these techniques offer reliable patterning of graphene materials, the performance is often limited due to agglomeration of graphene layers. Laser-based technologies proved to be innovative and scalable approaches for direct-write (maskless) fabrication of 3D graphene electrodes for on-chip functional devices. Fabricated electrode patterns are monolithic, binder-free, porous and easy to print. Furthermore, heteroatom doping can be done by controlling the composition of the precursor film and by lasing in specific gas environments. With the right selection of precursor material, patterns of multi layer electrode stacks, graphene-metal, and graphene-inorganic composites can also be fabricated through direct-write laser lithography. Irrespective of the initial precursor composition, it is possible to pattern graphene and graphene hybrids precisely and directly in a single step according to specific application requirements.

Despite its remarkable success so far, many challenges remain before this technology can be brought into the market. For instance, the resolution of laser techniques should be improved by employ-

ing fine-focused laser beams to allow high-resolution electrode patterns. In addition, there is a chance to make a large variety of electrodes, including composites of 2D materials, and heterostructures of LDG materials. These have not been sufficiently explored yet. Embedded electronics and energy storage devices may be developed through defocused laser beams. In this case, the desired graphitic patterning can be done inside the thickness of the substrate. Since it is possible to control the degree of graphitization, vertical multi-layer structures can be fabricated through graded laser parameters. Such modular multi-layer graphene can exhibit interesting properties when compared to uniform graphene stacked structure. More detailed doping studies should be carried out to modify the physicochemical properties of graphene-based electrodes. Fabrication of vertical graphene architectures should be studied to increase the LDG density in a given footprint area for improved areal performance metrics. Limited research was performed using LDG as anodes for mobile-ion batteries, including Al, Mg, Ca and so forth. Most recent studies have used bench-top laser processing, but there must be more effort to scale-up this process; for example, scalable manufacturing of graphitic electrodes through roll-to-roll approach, as illustrated in Fig. 17 [45]. This technology is viable for the commercialization of on-chip graphitic

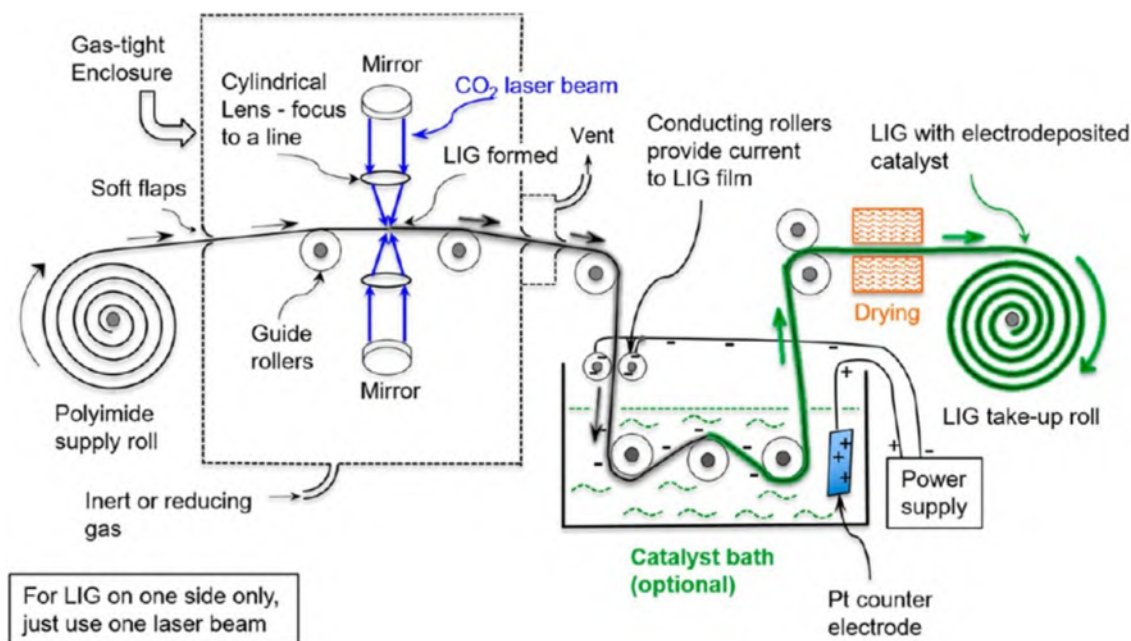


Fig. 17. Schematic illustration for roll-to-roll (R2R) manufacturing of graphitic electrodes on the PI sheet. Further, the hybrid material can be deposited using a catalyst bath (optional). Adapted with permission from reference [45]. Copyright 2018, American Chemical Society.

electrodes as sensors and small-scale energy storage components. Tour group has demonstrated 3D graphene foam synthesis using a modified, automated 3D printing process based on laminated object manufacturing [180]. Laser-derived graphitic deposits on PI sheets were glued together; subsequent laser irradiation on the bi-stack resulted in 3D graphene foam structures. This study bodes well for developing other 3D structured materials and embedded graphene circuits. Further, laser sintering of metal powder embedded in carbon precursor was demonstrated for the fabrication of porous 3D graphene architectures, done by consecutive addition of Ni/carbon precursor layers and sequential repetition of these steps. Finally, Ni was etched away to result in porous 3D graphene scaffolds [45].

Recently, Brousse et al. demonstrated the fabrication of RuO₂ micro-supercapacitors through laser scribing of ruthenium complexes spun cast on a PI substrate [181]. This study offers new possibilities to explore the fabrication of various metal oxide-, sulfide- or nitride-based electrodes for on-chip supercapacitors, sensors and electrocatalysts. It is also possible to develop a variety of hybrid or composite materials through laser scribing by choosing appropriate precursor materials and laser parameters. For example, flexible and transparent graphene circuits were also demonstrated using direct-write laser lithography [182].

In summary, LDG represents an emerging class of direct-write 3D printed electrodes that have been shown useful for various applications. Yet, the technology is in its early stages of development, and it is expected that fine control of material properties and discovery of new applications will continue in the future.

Acknowledgment

Research reported in this publication was supported by King Abdullah University of Science & Technology (KAUST).

References

- [1] K.S. Novoselov, A.K. Geim, S.V. Morozov, D. Jiang, Y. Zhang, S.V. Dubonos, I.V. Grigorieva, A.A. Firsov, *Science* 306 (2004) 666–669.
- [2] A.K. Geim, K.S. Novoselov, *Nat. Mater.* 6 (2007) 183–191.
- [3] D. Li, M.B. Müller, S. Gilje, R.B. Kaner, G.G. Wallace, *Nat. Nanotechnol.* 3 (2008) 101–105.
- [4] Y. Zhu, S. Murali, W. Cai, X. Li, J.W. Suk, J.R. Potts, R.S. Ruoff, *Adv. Mater.* 22 (2010) 3906–3924.
- [5] H.A. Becerril, J. Mao, Z. Liu, R.M. Stoltzberg, Z. Bao, Y. Chen, *ACS Nano* 2 (2008) 463–470.
- [6] L. Qu, Y. Liu, J.B. Baek, L. Dai, *ACS Nano* 4 (2010) 1321–1326.
- [7] F. Schwierz, *Nat. Nanotechnol.* 5 (2010) 487–496.
- [8] S. Bae, H. Kim, Y. Lee, X. Xu, J.S. Park, Y. Zheng, J. Balakrishnan, T. Lei, H.R. Kim, Y. Il Song, Y.J. Kim, K.S. Kim, B. Özyilmaz, J.H. Ahn, B.H. Hong, S. Iijima, *Nat. Nanotechnol.* 5 (2010) 574–578.
- [9] A.H.C. Neto, F. Guinea, N.M.R. Peres, K.S. Novoselov, A.K. Geim, *Rev. Mod. Phys.* 81 (2007) 109.
- [10] S. Stankovich, D.A. Dikin, R.D. Piner, K.A. Kohlhaas, A. Kleinhammes, Y.Y. Jia, Y. Wu, S.B.T. Nguyen, R.S. Ruoff, *Carbon* 45 (2007) 1558–1565.
- [11] V. Singh, D. Joung, L. Zhai, S. Das, S.I. Khondaker, S. Seal, *Prog. Mater. Sci.* 56 (2011) 1178–1271.
- [12] C. Lee, X. Wei, J.W. Kysar, J. Hone, *Science* 321 (2008) 385–388.
- [13] X. Li, W. Cai, J. An, S. Kim, J. Nah, D.X. Yang, R. Piner, A. Velamakanni, I. Jung, E. Tutuc, S.K. Banerjee, L. Colombo, R.S. Ruoff, *Science* 324 (2009) 1312–1314.
- [14] A.K. Geim, *Science* 324 (2009) 1530–1534.
- [15] C. Berger, Z. Song, T. Li, X. Li, A.Y. Ogbazghi, R. Feng, Z. Dai, A.N. Marchenkov, E.H. Conrad, P.N. First, W.A. De Heer, *J. Phys. Chem. B* 108 (2004) 19912–19916.
- [16] K.S. Novoselov, V.I. Fal'ko, L. Colombo, P.R. Gellert, M.G. Schwab, K. Kim, *Nature* 438 (2005) 197–200.
- [17] Q. Xiang, J. Yu, M. Jaroniec, *Chem. Soc. Rev.* 41 (2012) 782–796.
- [18] K.S. Novoselov, A.K. Geim, S.V. Morozov, D. Jiang, M.I. Katsnelson, I.V. Grigorieva, S.V. Dubonos, A.A. Firsov, *Nature* 438 (2005) 197–200.
- [19] Y. Zhang, Y.W. Tan, H.L. Stormer, P. Kim, *Nature* 438 (2005) 201–204.
- [20] S. Stankovich, D.A. Dikin, G.H.B. Dommett, K.M. Kohlhaas, E.J. Zimney, E.A. Stach, R.D. Piner, S.B.T. Nguyen, R.S. Ruoff, *Nature* 442 (2006) 282–286.
- [21] K.S. Kim, Y. Zhao, H. Jang, S.Y. Lee, J.M. Kim, K.S. Kim, J.H. Ahn, P. Kim, J.Y. Choi, B.H. Hong, *Nature* 457 (2009) 706–710.
- [22] A.A. Balandin, S. Ghosh, W. Bao, I. Calizo, D. Teweldebrhan, F. Miao, C.N. Lau, *Nano Lett.* 8 (2008) 902–907.
- [23] D. Wei, Y. Liu, Y. Wang, H. Zhang, L. Huang, G. Yu, *Nano Lett.* 9 (2009) 1752–1758.
- [24] Z.S. Wu, W. Ren, L. Wen, L. Gao, J. Zhao, Z. Chen, G. Zhou, F. Li, H.M. Cheng, *ACS Nano* 4 (2010) 3187–3194.
- [25] E.H. Hwang, S.D. Sarma, *Phys. Rev. B* 77 (2008), 115449.
- [26] L.A. Falkovsky, *J. Phys. Conf. Ser.* 129 (2008), 012004.
- [27] A. Züttel, P. Sudan, P. Mauron, P. Wenger, *Appl. Phys. A* 78 (2004) 941–946.
- [28] K.V. Emtsev, A. Bostwick, K. Horn, J. Jobst, G.L. Kellogg, L. Ley, J.L. McChesney, T. Ohta, S.A. Reshanov, J. Röhrl, E. Rotenberg, A.K. Schmid, D. Waldmann, H.B. Weber, T. Seyller, *Nat. Mater.* 8 (2009) 203–207.
- [29] A. Reina, X. Jia, J. Ho, D. Nezich, H. Son, V. Bulovic, M.S. Dresselhaus, K. Kong, *Nano Lett.* 9 (2009) 30–35.
- [30] J.W. Suk, A. Kitt, C.W. Magnuson, Y. Hao, S. Ahmed, J. An, A.K. Swan, B.B. Goldberg, R.S. Ruoff, *ACS Nano* 5 (2011) 6916–6924.

- [31] W. Choi, I. Lahiri, R. Seelaboyina, Y.S. Kang, Crit. Rev. Solid State Mater. Sci. 35 (2010) 52–71.
- [32] V. Georgakilas, J.N. Tiwari, K.C. Kemp, J.A. Perman, A.B. Bourlinos, K.S. Kim, R. Zboril, Chem. Rev. 116 (2016) 5464–5519.
- [33] Z. Chen, W. Ren, L. Gao, B. Liu, S. Pei, H.M. Cheng, Nat. Mater. 10 (2011) 424–428.
- [34] V.C. Tung, M.J. Allen, Y. Yang, R.B. Kaner, Nat. Nanotechnol. 4 (2009) 25–29.
- [35] W.S. Hummers, R.E. Offeman, J. Am. Chem. Soc. 80 (1958) 1339.
- [36] Y. Xu, K. Sheng, C. Li, G. Shi, ACS Nano 4 (2010) 4324–4330.
- [37] X. Yang, C. Cheng, Y. Wang, L. Qiu, D. Li, Science 341 (2013) 534–537.
- [38] S. Pei, H.M. Cheng, Carbon 50 (2012) 3210–3228.
- [39] S. Wang, P.K. Ang, Z. Wang, A.L.L. Tang, J.T.L. Thong, K.P. Loh, Nano Lett. 10 (2010) 92–98.
- [40] A.E. Jakus, E.B. Secor, A.L. Rutz, S.W. Jordan, M.C. Hersam, R.N. Shah, ACS Nano 9 (2015) 4636–4648.
- [41] H.P. Cong, X.C. Ren, P. Wang, S.H. Yu, ACS Nano 6 (2012) 2693–2703.
- [42] K. Chi, Z. Zhang, J. Xi, Y. Huang, F. Xiao, S. Wang, Y. Liu, ACS Appl. Mater. Interfaces 6 (2014) 16312–16319.
- [43] K. Fu, Y. Wang, C. Yan, Y. Yao, Y. Chen, J. Dai, S. Lacey, Y. Wang, J. Wan, T. Li, Z. Wang, Y. Xu, L. Hu, Adv. Mater. 28 (2016) 2587–2594.
- [44] M.F. El-Kady, V. Strong, S. Dubin, R.B. Kaner, Science 335 (2012) 1326–1330.
- [45] R. Ye, D.K. James, J.M. Tour, Acc. Chem. Res. 51 (2018) 1609–1620.
- [46] Z. Wei, D. Wang, S. Kim, S. Kim, Y. Hu, M.K. Yakes, W.A. De Heer, P.E. Sheehan, E. Riedo, Science 328 (2010) 1373–1376.
- [47] J. Cheng, C.S. Liu, S. Shang, D. Liu, W. Perrie, G. Dearden, K. Watkins, Opt. Laser Technol. 46 (2013) 88–102.
- [48] J. Song, F.Y. Kam, R.Q. Png, W.L. Seah, J.M. Zhuo, G.K. Lim, P.K.H. Ho, L.L. Chua, Nat. Nanotechnol. 8 (2013) 356–362.
- [49] N. Kurra, A.A. Sagade, G.U. Kurnarli, Adv. Funct. Mater. 21 (2011) 3836–3842.
- [50] F. Wakaya, T. Kurihara, N. Yurugi, S. Abo, M. Abe, M. Takai, Microelectron. Eng. 141 (2015) 203–206.
- [51] W. Gao, N. Singh, L. Song, Z. Liu, A.L.M. Reddy, L. Ci, R. Vajtai, Q. Zhang, B. Wei, P.M. Ajayan, Nat. Nanotechnol. 6 (2011) 496–500.
- [52] J. Lin, Z. Peng, Y. Liu, F. Ruiz-Zepeda, R. Ye, E.L.G. Samuel, M.J. Yacaman, B.I. Yakobson, J.M. Tour, Nat. Commun. 5 (2015) 5714.
- [53] X. Ye, J. Long, Z. Lin, H. Zhang, H. Zhu, M. Zhong, Carbon 68 (2014) 784–790.
- [54] A. Lamberti, M. Serrapède, G. Ferraro, M. Fontana, F. Perrucci, S. Bianco, A. Chiolerio, S. Bocchini, 2D Mater. 4 (2017), 035012.
- [55] A.T.T. Koh, Y.M. Foong, D.H.C. Chua, Appl. Phys. Lett. 97 (2010) 98–101.
- [56] K. Wang, G. Tai, K.H. Wong, S.P. Lau, W. Guo, AIP Adv. 1 (2011), 022141.
- [57] Y. Zhang, L. Guo, S. Wei, Y. He, H. Xia, Q. Chen, H.B. Sun, F.S. Xiao, Nano Today 5 (2010) 15–20.
- [58] S. Luo, P.T. Hoang, T. Liu, Carbon 96 (2016) 522–531.
- [59] W.A. de Heer, C. Berger, X. Wu, P.N. First, E.H. Conrad, X. Li, T. Li, M. Sprinkle, J. Hass, M.L. Sadowski, M. Potemski, G. Martinez, Solid State Commun. 143 (2007) 92–100.
- [60] A. Longo, R. Verucchi, L. Aversa, R. Tatti, A. Ambrosio, E. Orabona, U. Coscia, G. Carotenuto, P. Maddalena, Nanotechnology 28 (2017), 224002.
- [61] M. Qian, Y.S. Zhou, Y. Gao, J.B. Park, T. Feng, S.M. Huang, Z. Sun, L. Jiang, Y.F. Lu, Appl. Phys. Lett. 98 (2011), 173108.
- [62] B. Dorin, P. Parkinson, P. Scully, J. Mater. Chem. C 5 (2017) 4923–4930.
- [63] R. Arul, R.N. Oosterbeek, J. Robertson, G. Xu, J. Jin, M.C. Simpson, Carbon 99 (2016) 423–431.
- [64] R. Rahimi, M. Ochoa, W. Yu, B. Ziaie, ACS Appl. Mater. Interfaces 7 (2015) 4463–4470.
- [65] M.F. El-Kady, R.B. Kaner, Nat. Commun. 4 (2013) 1475.
- [66] M.F. El-Kady, M. Ihns, M. Li, J.Y. Hwang, M.F. Mousavi, L. Chaney, A.T. Lech, R.B. Kaner, Proc. Natl. Acad. Sci. 112 (2015) 4233–4238.
- [67] J.Y. Hwang, M.F. El-Kady, Y. Wang, L. Wang, Y. Shao, K. Marsh, J.M. Ko, R.B. Kaner, Nano Energy 18 (2015) 57–70.
- [68] L.V. Thekkere, B. Jia, Y. Zhang, L. Qiu, D. Li, M. Gu, Appl. Phys. Lett. 107 (2015) 2013–2016.
- [69] V. Strong, S. Dubin, M.F. El-Kady, A. Lech, Y. Wang, B.H. Weiller, R.B. Kaner, ACS Nano 6 (2012) 1395–1403.
- [70] P. Nayak, Q. Jiang, N. Kurra, X. Wang, U. Buttner, H.N. Alshareef, J. Mater. Chem. A 5 (2017) 20422–20427.
- [71] S.P. Singh, Y. Li, J. Zhang, J.M. Tour, C.J. Arnusch, ACS Nano 12 (2018) 289–297.
- [72] L.Q. Tao, H. Tian, Y. Liu, Z.Y. Ju, Y. Pang, Y.Q. Chen, D.Y. Wang, X.G. Tian, J.C. Yan, N.Q. Deng, Y. Yang, T.L. Ren, Nat. Commun. 8 (2017) 14579.
- [73] P. Nayak, N. Kurra, C. Xia, H.N. Alshareef, Adv. Electron. Mater. 2 (2016), 1600185.
- [74] Y. Chyan, R. Ye, Y. Li, S.P. Singh, C.J. Arnusch, J.M. Tour, ACS Nano 12 (2018) 2176–2183.
- [75] R. Ye, Y. Chyan, J. Zhang, Y. Li, X. Han, C. Kittrell, J.M. Tour, Adv. Mater. 29 (2017), 1702211.
- [76] R. Ye, X. Han, D.V. Kosynkin, Y. Li, C. Zhang, B. Jiang, A.A. Martí, J.M. Tour, ACS Nano 12 (2018) 1083–1088.
- [77] X. Wang, H. Tian, M.A. Mohammad, C. Li, C. Wu, Y. Yang, T.L. Ren, Nat. Commun. 6 (2015) 7767.
- [78] D.Y. Wang, L.Q. Tao, Y. Liu, T.Y. Zhang, Y. Pang, Q. Wang, S. Jiang, Y. Yang, T.L. Ren, Nanoscale 8 (2016) 20090–20095.
- [79] H. Tian, Y. Yang, D. Xie, Y.L. Cui, W.T. Mi, Y. Zhang, T.L. Ren, Sci. Rep. 4 (2014) 1398.
- [80] H. Tian, Y. Shu, X.F. Wang, M.A. Mohammad, Z. Bie, Q.Y. Xie, C. Li, W.T. Mi, Y. Yang, T.L. Ren, Sci. Rep. 5 (2015) 8603.
- [81] H. Tian, C. Li, M.A. Mohammad, Y.L. Cui, W.T. Mi, Y. Yang, D. Xie, T.L. Ren, ACS Nano 8 (2014) 5883–5890.
- [82] H. Tian, H.Y. Chen, T.L. Ren, C. Li, Q.T. Xue, M.A. Mohammad, C. Wu, Y. Yang, H.S.P. Wong, Nano Lett. 14 (2014) 3214–3219.
- [83] L.Q. Tao, D.Y. Wang, H. Tian, Z.Y. Ju, Y. Liu, Y. Pang, Y.Q. Chen, Y. Yang, T.L. Ren, Nanoscale 9 (2017) 8266–8273.
- [84] L.Q. Tao, Y. Liu, Z.Y. Ju, H. Tian, Q.Y. Xie, Y. Yang, T.L. Ren, Nanomaterials 6 (2016) 112.
- [85] M.A. Mohammad, H. Tian, Z.Y. Ju, H.M. Zhao, C. Li, M.A. Mohammad, L.Q. Tao, Y. Pang, X.F. Wang, T.Y. Zhang, Y. Yang, T.L. Ren, Carbon 109 (2016) 173–181.
- [86] S.Y. Lin, T.Y. Zhang, Q. Lu, D.Y. Wang, Y. Yang, X.M. Wu, T.L. Ren, RSC Adv. (2017) 27001–27006.
- [87] J.B. Park, W. Xiong, Y. Gao, M. Qian, Z.Q. Xie, M. Mitchell, Y.S. Zhou, G.H. Han, L. Jiang, Y.F. Lu, Appl. Phys. Lett. 98 (2011) 123109.
- [88] H. Teoh, Y. Tao, E.S. Tok, G.W. Ho, C.H. Sow, J. Appl. Phys. 112 (2012), 064309.
- [89] A.C. Ferrari, J.C. Meyer, V. Scardaci, C. Casiraghi, M. Lazzeri, F. Mauri, S. Pisacane, D. Jiang, K.S. Novoselov, S. Roth, A.K. Geim, Phys. Rev. Lett. 97 (2006) 41–47.
- [90] M.S. Dresselhaus, A. Jorio, M. Hofmann, G. Dresselhaus, R. Saito, Nano Lett. 10 (2010) 751–758.
- [91] D.S. Knight, W.B. White, J. Mater. Res. 4 (1989) 385–393.
- [92] R. Trusovas, G. Račukaitis, G. Niaura, J. Barkauskas, G. Valušis, R. Pauliukaite, Adv. Opt. Mater. 4 (2016) 37–65.
- [93] Z.L. Wang, Nano Today 5 (2010) 512–514.
- [94] M. Beidaghi, Y. Gogotsi, Energy Environ. Sci. 7 (2014) 867–884.
- [95] G. Xiong, C. Meng, R.G. Reifenberger, P.P. Irazoqui, T.S. Fisher, Electroanalysis 26 (2014) 30–51.
- [96] D.R. Rolison, J.W. Long, J.C. Lytle, A.E. Fischer, C.P. Rhodes, T.M. McEvoy, M.E. Bourg, A.M. Lubers, Chem. Soc. Rev. 38 (2009) 226–252.
- [97] J.W. Long, B. Dunn, D.R. Rolison, H.S. White, Chem. Rev. 104 (2004) 4463–4492.
- [98] Q. Jiang, C. Wu, Z.J. Wang, A.C. Wang, J.H. He, Z.L. Wang, H.N. Alshareef, Nano Energy 45 (2018) 266–272.
- [99] S. Niu, X. Wang, F. Yi, Y.S. Zhou, Z.L. Wang, Nat. Commun. 6 (2015) 8975.
- [100] R.Z. Li, R. Peng, K.D. Kihm, S. Bai, D. Bridges, U. Tumuluri, Z. Wu, T. Zhang, G. Compagnini, Z. Feng, A. Hu, Energy Environ. Sci. 9 (2016) 1458–1467.
- [101] D. Qi, Y. Liu, Z. Liu, L. Zhang, X. Chen, Adv. Mater. 29 (2017), 1602802.
- [102] N.A. Kyerematem, T. Brousse, D. Pech, Nat. Nanotechnol. 12 (2017) 7–15.
- [103] D. Pech, M. Brunet, P.L. Taberna, P. Simon, N. Fabre, F. Mesnilgrente, V. Conédéra, H. Durou, J. Power Sources 195 (2010) 1266–1269.
- [104] D. Pech, M. Brunet, H. Durou, P. Huang, V. Mochalin, Y. Gogotsi, P.L. Taberna, P. Simon, Nat. Nanotechnol. 5 (2010) 651–654.
- [105] J. Chmiola, P.L.T. Celine Largeot, P. Simon, Y. Gogotsi, Science 328 (2010) 480–483.
- [106] M. Beidaghi, C. Wang, Adv. Funct. Mater. 22 (2012) 4501–4510.
- [107] Z.S. Wu, K. Parvez, X. Feng, K. Müllen, Nat. Commun. 4 (2013) 2487.
- [108] Z.S. Wu, X. Feng, H.M. Cheng, Natl. Sci. Rev. 1 (2014) 277–292.
- [109] A. Tyagi, K.M. Tripathi, R.K. Gupta, J. Mater. Chem. A 3 (2015) 22507–22541.
- [110] F. Bonaccorso, L. Colombo, G. Yu, M. Stoller, V. Tozzini, A.C. Ferrari, R.S. Ruoff, V. Pellegrini, Science 347 (2015), 1246501.
- [111] L. Peng, Y. Zhu, D. Chen, R.S. Ruoff, G. Yu, Adv. Energy Mater. 6 (2016), 1600025.
- [112] Y. Zhu, L. Peng, Z. Fang, C. Yan, X. Zhang, G. Yu, Adv. Mater. 30 (2018), 1706347.
- [113] Z. Peng, J. Lin, R. Ye, E.L.G. Samuel, J.M. Tour, ACS Appl. Mater. Interfaces 7 (2015) 3414–3419.
- [114] W. Zhang, Y. Lei, F. Ming, Q. Jiang, P.M.F.J. Costa, H.N. Alshareef, Adv. Energy Mater. 1 (2018), 1801840.
- [115] Q. Jiang, N. Kurra, M. Alhabeb, Y. Gogotsi, H.N. Alshareef, Adv. Energy Mater. 8 (2018), 1703043.
- [116] L. Li, J. Zhang, Z. Peng, Y. Li, C. Gao, Y. Ji, R. Ye, N.D. Kim, Q. Zhong, Y. Yang, H. Fei, G. Ruan, J.M. Tour, Adv. Mater. 28 (2016) 838–845.
- [117] S.E. Moosavifard, J. Shamsi, M.K. Altafi, Z.S. Moosavifard, Chem. Commun. (Camb.) 52 (2016) 13140–13143.
- [118] Z. Peng, R. Ye, J.A. Mann, D. Zakhidov, Y. Li, P.R. Smalley, J. Lin, J.M. Tour, ACS Nano 9 (2015) 5868–5875.
- [119] S. Wang, Y. Yu, R. Li, G. Feng, Z. Wu, G. Compagnini, A. Gulino, Z. Feng, A. Hu, Electrochim. Acta 241 (2017) 153–161.
- [120] S. Wang, Y. Yu, D. Ma, D. Bridges, G. Feng, A. Hu, J. Laser Appl. 29 (2017), 022203.
- [121] L. Guo, Y.L. Zhang, D.D. Han, H.B. Jiang, D. Wang, X. Bin Li, H. Xia, J. Feng, Q.D. Chen, H.B. Sun, Adv. Opt. Mater. 2 (2014) 120–125.
- [122] X.Y. Fu, D.L. Chen, Y. Liu, H.B. Jiang, H. Xia, H. Ding, Y.L. Zhang, ACS Appl. Nano Mater. 1 (2018) 777–784.
- [123] V. Etacheri, R. Marom, R. Elazari, G. Salitra, D. Aurbach, Energy Environ. Sci. 4 (2011) 3243–3262.
- [124] F. Zhang, E. Alhajji, Y. Lei, N. Kurra, H.N. Alshareef, Adv. Energy Mater. 8 (2018), 1800353.
- [125] H. Wang, C. Zhu, D. Chao, Q. Yan, H.J. Fan, Adv. Mater. 29 (2017), 1702093.
- [126] M. Labib, E.H. Sargent, S.O. Kelley, Chem. Rev. 116 (2016) 9001–9090.
- [127] C.E. Banks, R.G. Compton, Analyst 131 (2006) 15–21.
- [128] S. Wu, Q. He, C. Tan, Y. Wang, H. Zhang, Small 9 (2013) 1160–1172.
- [129] C.E. Banks, R.G. Compton, Anal. Sci. 21 (2005) 1263–1268.
- [130] A.P.F. Turner, Science 290 (2000) 1315–1317.
- [131] P. Nayak, B. Anbarasan, S. Ramaprabhu, J. Phys. Chem. C 117 (2013) 13202–13209.

- [132] X.C. Dong, H. Xu, X.W. Wang, Y.X. Huang, M.B. Chan-Park, H. Zhang, L.H. Wang, W. Huang, P. Chen, *ACS Nano* 6 (2012) 3206–3213.
- [133] Y. Huang, X. Dong, Y. Shi, C.M. Li, L.J. Li, P. Chen, *Nanoscale* 2 (2010) 1485–1488.
- [134] M. Zhou, Y. Zhai, S. Dong, *Anal. Chem.* 81 (2009) 5603–5613.
- [135] K. Vijayaraj, S.W. Hong, S.H. Jin, S.C. Chang, D.S. Park, *Anal. Methods* 8 (2016) 6974–6981.
- [136] X. Dong, Y. Shi, W. Huang, P. Chen, L.J. Li, *Adv. Mater.* 22 (2010) 1649–1653.
- [137] K. Griffiths, C. Dale, J. Hedley, M.D. Kowal, R.B. Kaner, N. Keegan, *Nanoscale* 6 (2014) 13613–13622.
- [138] D.A.C. Brownson, S.A. Varey, F. Hussain, S.J. Haigh, C.E. Banks, *Nanoscale* 6 (2014) 1607–1621.
- [139] T.J. Davies, R.R. Moore, C.E. Banks, R.G. Compton, *J. Electroanal. Chem.* 574 (2004) 123–152.
- [140] E.P. Randviir, D.A.C. Brownson, M. Gómez-Mingot, D.K. Kampouris, J. Iniesta, C.E. Banks, *Nanoscale* 4 (2012) 6470–6480.
- [141] C. Bosch-Navarro, Z.P.L. Laker, J.P. Rourke, N.R. Wilson, *Phys. Chem. Chem. Phys.* 17 (2015) 29628–29636.
- [142] Y. Wang, Z. Li, J. Wang, J. Li, Y. Lin, *Trends Biotechnol.* 29 (2011) 205–212.
- [143] C. Fenzi, P. Nayak, T. Hirsch, O.S. Wolfbeis, H.N. Alshareef, A.J. Baeumner, *ACS Sens.* 2 (2017) 616–620.
- [144] W.R. de Araujo, C.M.R. Frasson, W.A. Ameku, J.R. Silva, L. Angnes, T.R.L.C. Paixão, *Angew. Chem. Int. Ed.* 56 (2017) 15113–15117.
- [145] S. Lin, W. Feng, X. Miao, X. Zhang, S. Chen, Y. Chen, W. Wang, Y. Zhang, *Biosens. Bioelectron.* 110 (2018) 89–96.
- [146] F. Tehrani, B. Bavarian, *Sci. Rep.* 6 (2016) 27975.
- [147] Z. Zhang, M. Song, J. Hao, K. Wu, C. Li, C. Hu, *Carbon* 127 (2018) 287–296.
- [148] D.C. Vanegas, L. Patiño, C. Mendez, D.A. de Oliveira, A.M. Torres, C.L. Gomes, E.S. McLamore, *Biosensors* 8 (2018) 42.
- [149] R. Rahimi, M. Ochoa, A. Tamayol, S. Khalili, A. Khademhosseini, B. Ziaie, *ACS Appl. Mater. Interfaces* 9 (2017) 9015–9023.
- [150] M.E.E. Alahi, A. Nag, S.C. Mukhopadhyay, L. Burkitt, *Sens. Actuator A: Phys.* 269 (2018) 79–90.
- [151] C. Cheng, S. Wang, J. Wu, Y. Yu, R. Li, S. Eda, J. Chen, G. Feng, B. Lawrie, A. Hu, *ACS Appl. Mater. Interfaces* 8 (2016) 17784–17792.
- [152] A. Nag, S.C. Mukhopadhyay, J. Kosel, *Sens. Actuators* 264 (2017) 107–116.
- [153] R. Michalsky, Y.J. Zhang, A.A. Peterson, *ACS Catal.* 4 (2014) 1274–1278.
- [154] S. Fu, C. Zhu, J. Song, M.H. Engelhard, X. Li, D. Du, Y. Lin, *ACS Energy Lett.* 1 (2016) 792–796.
- [155] F. Ming, H. Liang, H. Shi, X. Xu, G. Mei, Z. Wang, *J. Mater. Chem. A* 4 (2016) 15148–15155.
- [156] W. Zhou, J. Zhou, Y. Zhou, J. Lu, K. Zhou, L. Yang, Z. Tang, L. Li, S. Chen, *Chem. Mater.* 27 (2015) 2026–2032.
- [157] H. Deng, C. Zhang, Y. Xie, T. Tumlin, L. Giri, S.P. Karna, J. Lin, *J. Mater. Chem. A* 4 (2016) 6824–6830.
- [158] T.Y. Ma, S. Dai, S.Z. Qiao, *Mater. Today* 19 (2016) 265–273.
- [159] L. Zhang, J. Xiao, H. Wang, M. Shao, *ACS Catal.* 7 (2017) 7855–7865.
- [160] R. Ye, Z. Peng, T. Wang, Y. Xu, J. Zhang, Y. Li, L.G. Nilewski, J. Lin, J.M. Tour, *ACS Nano* 9 (2015) 9244–9251.
- [161] J. Zhang, M. Ren, L. Wang, Y. Li, B.I. Yakobson, J.M. Tour, *Adv. Mater.* 30 (2018), 1707319.
- [162] J. Zhang, C. Zhang, J. Sha, H. Fei, Y. Li, J.M. Tour, *ACS Appl. Mater. Interfaces* 9 (2017) 26840.
- [163] H. Deng, C. Zhang, Y. Xie, T. Tumlin, L. Giri, S.P. Karna, J. Lin, *J. Mater. Chem. A* 4 (2016) 6824–6830.
- [164] J.Y. Lu, X.X. Zhang, Q.Y. Zhu, F.R. Zhang, W.T. Huang, X.Z. Ding, L.Q. Xia, H.Q. Luo, N.B. Li, *ACS Appl. Mater. Interfaces* 10 (2018) 17704–17713.
- [165] H. Tian, Y. Shu, Y.-L. Cui, W.-T. Mi, Y. Yang, D. Xie, T.-L. Ren, *Nanoscale* 6 (2014) 699–705.
- [166] C. Zhang, Y. Xie, H. Deng, T. Tumlin, C. Zhang, J.W. Su, P. Yu, J. Lin, *Small* 13 (2017), 1604197.
- [167] J. Li, S.S. Delektora, P. Zhang, S. Yang, M.R. Lohe, X. Zhuang, X. Feng, M. Östling, *ACS Nano* 11 (2017) 8249–8256.
- [168] Y.Q. Jiang, Q. Zhou, L. Lin, *IEEE 22nd Int. Conf. on MEMS*, 2009, pp. 587–590.
- [169] J. Lin, C. Zhang, Z. Yan, Y. Zhu, Z. Peng, R.H. Hauge, D. Natelson, J.M. Tour, *Nano Lett.* 13 (2013) 72–78.
- [170] L.M. Miller, P.K. Wright, C.C. Ho, J.W. Evans, P.C. Shafer, R. Ramesh, *Proc. IEEE ECCE 30* (2009) 2627–2634.
- [171] X. Dong, X. Wang, L. Wang, H. Song, H. Zhang, W. Huang, P. Chen, *ACS Appl. Mater. Interfaces* 4 (2012) 3129–3133.
- [172] S. Lin, W. Feng, X. Miao, X. Zhang, S. Chen, Y. Chen, W. Wang, Y. Zhang, *Biosens. Bioelectron.* 110 (2018) 89–96.
- [173] J. Song, L. Xu, C. Zhou, R. Xing, Q. Dai, D. Liu, H. Song, *ACS Appl. Mater. Interfaces* 5 (2013) 12928–12934.
- [174] D. Jiang, Q. Liu, K. Wang, J. Qian, X. Dong, Z. Yang, X. Du, B. Qiu, *Biosens. Bioelectron.* 54 (2014) 273–278.
- [175] Y. Qiao, Y. Wang, H. Tian, M. Li, J. Jian, Y. Wei, Y. Tian, D. Wang, Y. Pang, X. Geng, X. Wang, Y. Zhao, H. Wang, N. Deng, M. Jian, Y. Zhang, R. Liang, Y. Yang, T.L. Ren, *ACS Nano* 12 (2018) 8839–8846.
- [176] J. Zhao, G. Wang, R. Yang, X. Lu, M. Cheng, C. He, G. Xie, J. Meng, D. Shi, G. Zhang, *ACS Nano* 9 (2015) 1622–1629.
- [177] X.W. Fu, Z.M. Liao, J.X. Zhou, Y.B. Zhou, H.C. Wu, R. Zhang, G. Jing, J. Xu, X. Wu, W. Guo, D. Yu, *Appl. Phys. Lett.* 99 (2014) 213107.
- [178] X. Li, T. Yang, Y. Yang, J. Zhu, L. Li, F.E. Alam, X. Li, H. Cheng, C. Lin, Y. Fang, H. Zhu, *Adv. Funct. Mater.* 26 (2016) 1322–1329.
- [179] M.B. Coskun, A. Akbari, D.T.H. Lai, A. Neild, M. Majumder, T. Alan, *ACS Appl. Mater. Interfaces* 8 (2016) 22501–22505.
- [180] D.X. Luong, A.K. Subramanian, G.A.L. Silva, J. Yoon, S. Cofer, K. Yang, P.S. Owuor, T. Wang, Z. Wang, J. Lou, P.M. Ajayan, J.M. Tour, *Adv. Mater.* 30 (2018), 1707416.
- [181] K. Brousse, S. Nguyen, A. Gillet, S. Pinaud, R. Tan, A. Meffre, K. Soulantica, B. Chaudret, P.L. Taberna, M. Respaud, P. Simon, *Electrochim. Acta* 281 (2018) 816–821.
- [182] X. Dai, J. Wu, Z. Qian, H. Wang, J. Jian, Y. Cao, M.H. Rummeli, Q. Yi, H. Liu, G. Zou, *Sci. Adv.* 2 (2016), 1601574.



Dr. Narendra Kurra obtained his master's degree from School of Chemistry, University of Hyderabad, India (2008) and PhD from Jawaharlal Nehru Centre for Advanced Scientific Research (JNCASR), India (2013). He was working as a postdoctoral fellow at King Abdullah University of Science & Technology (KAUST). His research interests include energy storage across multiple length scales employing functional nanomaterials.



Qiu Jiang obtained his bachelor degree from University of Science and Technology of China. He is currently a PhD candidate of the Materials Science and Engineering program at KAUST. His research interests focus on fabricating on-chip energy storage devices employing direct write and conventional lithography techniques.



Dr. Pranati Nayak obtained her Ph.D. Dept. of Physics, Indian Institute of Technology Madras, India (2015) followed by a post-doctoral experience in Prof. Husam N. Alshareef's group at KAUST. Currently she is working as a DST Inspire Faculty at CSIR-Central Electrochemical Research Institute (CSIR-CECRI), India. Her research interests are on 2D nanomaterials for biosensing applications.



Dr. Husam Alshareef is a Professor of Materials Science & Engineering at King Abdullah University of Science & Technology (KAUST). He obtained his Ph.D. at North Carolina State University, USA, followed by a post-doctoral appointment at Sandia National Laboratory. Prof. Alshareef spent 11 years in the semiconductor industry where he developed materials and processes for integrated circuit fabrication. His group is interested in developing functional nanomaterials for electronics and energy applications.